

# On the relation between the 0.7-anomaly and the Kondo effect: Geometric Crossover between a Quantum Point Contact and a Kondo Quantum Dot

Jan Heyder,<sup>1,2</sup> Florian Bauer,<sup>1,2</sup> Enrico Schubert,<sup>1</sup> David Borowsky,<sup>1</sup>  
Dieter Schuh,<sup>3</sup> Werner Wegscheider,<sup>4</sup> Jan von Delft,<sup>1,2</sup> and Stefan Ludwig<sup>1</sup>

<sup>1</sup>*Center for NanoScience and Fakultät für Physik, Ludwig-Maximilians-Universität München,  
Geschwister-Scholl-Platz 1, 80539 München, Germany*

<sup>2</sup>*Arnold Sommerfeld Center for Theoretical Physics,  
Ludwig-Maximilians-Universität München, Theresienstrasse 37, D-80333 München, Germany*

<sup>3</sup>*Institut für Angewandte Physik, Universität Regensburg, D-93040 Regensburg, Germany*

<sup>4</sup>*Laboratory for Solid State Physics, ETH Zürich, CH-8093 Zürich, Switzerland*

(Dated: August 16, 2021)

Quantum point contacts (QPCs) and quantum dots (QDs), two elementary building blocks of semiconducting nanodevices, both exhibit famously anomalous conductance features: the 0.7-anomaly in the former case, the Kondo effect in the latter. For both the 0.7-anomaly and the Kondo effect, the conductance shows a remarkably similar low-energy dependence on temperature  $T$ , source-drain voltage  $V_{sd}$  and magnetic field  $B$ . In a recent publication [F. Bauer *et al.*, Nature, **501**, 73 (2013)], we argued that the reason for these similarities is that both a QPC and a KQD feature *spin fluctuations* that are induced by the sample geometry, confined in a small spatial regime, and enhanced by interactions. Here we further explore this notion experimentally and theoretically by studying the geometric crossover between a QD and a QPC, focussing on the  $B$ -field dependence of the conductance. We introduce a one-dimensional model that reproduces the essential features of the experiments, including a smooth transition between a Kondo QD and a QPC with 0.7-anomaly. We find that in both cases the anomalously strong negative magnetoconductance goes hand in hand with strongly enhanced local spin fluctuations. Our experimental observations include, in addition to the Kondo effect in a QD and the 0.7-anomaly in a QPC, Fano interference effects in a regime of coexistence between QD and QPC physics, and Fabry-Perot-type resonances on the conductance plateaus of a clean QPC. We argue that Fabry-Perot-type resonances occur generically if the electrostatic potential of the QPC generates a flatter-than-parabolic barrier top.

## I. INTRODUCTION

A QPC is a narrow one-dimensional (1D) constriction and a QD a small isolated puddle of charges, patterned in a two-dimensional electron system (2DES), e. g. by applying voltages to local gates. Being key ingredients of semiconductor-based quantum circuits, much effort has been devoted to understand their behavior at a fundamental level. Here, we investigate the geometric crossover between a QPC and a QD. The motivation for this study is to shed light on similarities and differences between the 0.7-anomaly exhibited by the conductance of a QPC, and the Kondo effect found in a Kondo quantum dot (KQD) that hosts an odd number of electrons and hence contains a localized spin.

The linear conductance  $G(V_c)$  of a QPC is famously quantized in units of  $G_Q = 2e^2/h$ , when measured as function of the gate voltage  $V_c$  defining the channel width<sup>1-3</sup>. The 0.7-anomaly is observed as an additional shoulder when the dimensionless conductance,  $g = G/G_Q$ , reaches the value  $g \simeq 0.7$  in the first conductance step<sup>4-14</sup>. It shows strikingly anomalous behavior as function of temperature ( $T$ ), magnetic field ( $B$ ) and source-drain voltage ( $V_{sd}$ ), which can not be explained within a non-interacting model. The *low-energy*  $T$ -,  $B$ - and  $V_{sd}$ -dependencies of the 0.7-anomaly are similar to those of a KQD<sup>15-22</sup> at excitation energies well below its Kondo temperature,  $T_K$ : for both QPC and KQD,

the linear conductance strongly decreases with increasing  $B$  and  $T$ , while the non-linear conductance shows a zero-bias peak as function of  $V_{sd}$ , that splits into two sub-peaks with increasing  $B$ . We will call this similar behavior the “0.7-Kondo-similarity” (.7KS). To explain it, Meir and collaborators<sup>23-25</sup> have argued that a “quasi-bound state” in the QPC, predicted via spin-density-functional theory, harbors a localized spin that causes Kondo-like conductance anomalies.

We have recently proposed a scenario that explains the microscopic origin of the 0.7-anomaly and of the .7KS without invoking a localized spin<sup>14</sup>. In a nutshell, we argue that the 0.7-anomaly is a direct consequence of a “van Hove ridge”, i. e. a smeared van Hove peak in the local density of states (LDOS) at the bottom of the lowest 1D sub-band of the QPC, whose shape follows that of the QPC potential barrier. Invoking a semi-classical picture, the LDOS is inversely proportional to the velocity of an electron with given energy at a given position; the van Hove ridge, which corresponds to a locally enhanced LDOS, thus reflects the fact that electrons are being slowed down while they cross the 1D barrier constituting the QPC. The slow electrons experience strongly enhanced mutual interactions. When the QPC barrier is tuned to lie just below the chemical potential, transport properties are significantly affected by these strongly enhanced electron interactions. In Ref. 14 we have shown that this amplification of interaction effects is sufficient

to fully explain the 0.7-anomaly.

The above-mentioned two scenarios for explaining the 0.7-anomaly, evoking a quasi-localized state or a van Hove ridge, respectively, have an important common feature, namely that in both cases, the physics is governed by slow electrons above the barrier top. In this regard, it is not surprising that both scenarios are compatible in their predictions for the low-energy behavior of the 0.7-anomaly, which, as mentioned above, is similar to that of the Kondo effect. In Ref. 14, we attributed this .7KS to the fact that both a KQD and a QPC involve a spin-singlet ground state featuring *spatially confined spin fluctuations*. While for a KQD they are associated with the screening of a truly localized spin, for a QPC they result from the extended but curved structure of the van Hove ridge and include a large number of spins. In both cases, these spin fluctuations are characterized by an exponentially small energy scale, called  $B_*$  in Ref. 14, which goes hand in hand with an enhanced local spin susceptibility. For a KQD this low-energy scale corresponds to the Kondo temperature,  $T_K$ . The .7KS pertains to energies well below  $B_*$ ; we have argued in Ref. 14 that it results from the fact that for such low energies, both a KQD and a QPC show Fermi-liquid behavior of the type associated with quasi-particles experiencing spatially localized interactions. For the Kondo effect, a corresponding Fermi-liquid theory has been worked out by Nozières<sup>26</sup>; doing the same for a QPC would be an interesting challenge for the future.

Though slow electrons form the common ground for both the van Hove ridge scenario and quasi-localized state scenario, the two scenarios differ substantially in their microscopic description of the slow electrons' dynamics. The van Hove ridge scenario describes them via the LDOS, thus incorporating the geometric shape of the barrier. In contrast, the quasi-localized state scenario describes them more simplistically in terms of a magnetic moment, i.e. a truly localized state, thus arriving at a seemingly simpler model, akin to the single-impurity Anderson model. This apparent simplification, however, comes at a price: the physics of the Anderson model involves a free local moment high energies, and Fermi-liquid behavior emerges only at low energies, when the local moment is screened. For a QPC such a “detour” (first evoke a local moment, then argue that it is screened) is in our opinion not needed: in our van Hove ridge scenario, Fermi-liquid behavior is present *a priori*. Moreover, in Ref. 14 we have found no indications that a smooth parabolic barrier hosts a discrete, truly localized spin, and no similarities (in our experimental results or theoretical predictions) between the Kondo effect and the 0.7-anomaly at high energies ( $\gtrsim B_*$ ), where the Kondo effect is governed by an unscreened local moment. This shows that when the “slow electrons” in a QPC are probed at energies  $\gtrsim B_*$ , they do behave differently from the magnetic moment in a KQD. (In Sec. VI we offer additional evidence for this conclusion by comparing the behavior of the magnetization of a KQD and a QPC at

large magnetic fields.)

The differences between a KQD and a QPC come to the fore very explicitly in the functional dependence of the low-energy scale  $B_*$  on system parameters such as the gate voltage and the interaction strength (discussed in detail in Sec. IV C below). For a KQD, the scale  $B_*^{\text{KQD}}$  can not meaningfully be defined in the absence of interactions (since then no local moment forms), and  $\ln B_*^{\text{KQD}}$  depends quadratically on gate voltage<sup>19,22,27</sup>. For a QPC, in contrast,  $B_*^{\text{QPC}}$  can be meaningfully defined even in the absence of interactions, and  $\ln B_*^{\text{QPC}}$  depends linearly on gate voltage. When interactions are turned on,  $B_*^{\text{QPC}}$  is reduced strongly, but its functional dependence on gate voltage hardly changes (see Ref. 14, Sec. S-5).

The present paper aims to elaborate the relation between local spin fluctuations and the .7KS in more detail, and, more generally, to analyse the similarities and differences between the Kondo effect and the 0.7-anomaly, focussing on their dependence on magnetic field at low temperature, in equilibrium. We experimentally and theoretically study the smooth *geometric crossover* between a KQD and a QPC, and hence between the Kondo effect and the 0.7-anomaly. Experimentally, we measure the conductance throughout the QD-QPC crossover using a highly tunable nanostructure tailor-made for this purpose. In our theoretical work, we consider a 1D model with local interactions and a smooth potential barrier, similar to that used in Ref. 14, but now tune the shape of the potential barrier in such a way that it smoothly crosses over between a single barrier, representing a QPC, and a double barrier, representing a KQD. We use the functional renormalization group (fRG)<sup>28-31</sup> to calculate how transport and thermodynamic properties at  $T = 0$  change during this crossover. This allows us to track the extent to which features characteristic for Kondo correlations do or do not survive in the QPC regime. A central finding is that the strongly enhanced local spin susceptibility in the center of the system that is found for both a QPC and a KQD goes hand in hand with an anomalously strong magnetic field dependence of the conductance. This is actually not surprising, since a large spin susceptibility indicates a strong depletion of that spin species that is energetically disfavoured in the presence of a small magnetic field. Our analysis pinpoints the enhanced local spin susceptibility as the common feature of both systems that underlies the .7KS regarding its dependence on magnetic field.

The paper is organized as follows: Sec. II describes our experimental setup and our measurements for the QD-QPC crossover. Sec. III presents the model by which we describe this crossover, discusses how the geometry of the QPC or QD barrier influences the noninteracting LDOS and noninteracting transmission probability, and summarizes the key elements of our fRG approach for treating interactions. Sec. IV compares fRG results and experimental data for this crossover, showing that our model captures its main features in a qualitatively correct manner. Sec. V presents the results of fRG calculations for

local properties, such as the local density, magnetization and spin susceptibility for both a QPC and a QKD, and for the spin susceptibility during the QPC-QD crossover, which very clearly reveals the origin of the .7KS. Sec. VI presents fRG results on the evolution of the magnetization with  $\tilde{B}$ , highlighting the difference between a QKD and QPC when probed at energies beyond  $B_*$ . Sec. VII offers a summary and outlook. An appendix presents and discusses a movie with fRG results that show how the conductance evolves with magnetic field during the QD-QPC crossover.

## II. EXPERIMENTAL SETUP

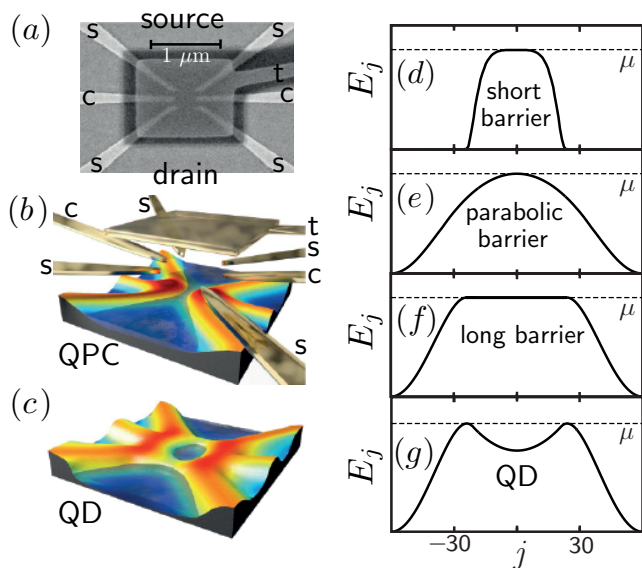


Figure 1. Geometric crossover between QPC and QD – sample and shape of effective potential. (a) Scanning electron microscope picture of the gate layout, which features a top gate at voltage  $V_t$ , two central gates at voltage  $V_c$ , and four side gates at voltage  $V_s$ . Negative voltages  $V_c$  and  $V_s$  deplete the 2DES 85 nm beneath the sample surface, inducing a tunable effective electrostatic potential landscape there. (b,c) Artist's depiction of this landscape for a QPC and QD, respectively [red/yellow: high electrostatic potential; blue: low potential, Fermi sea darkened; golden structures at top of (b): gates]. (d-g) The effective potential  $E_j$  of the Hamiltonian given in Eq. (1), shown for four different choices of the barrier shape (black lines), tuned by adjusting the central barrier height  $\tilde{V}_c = E_{j=0} - \varepsilon_F$ , the side barrier height  $\tilde{V}_s$  (with  $\tilde{V}_{c,s} \propto -|e|V_{c,s}$ ), and the barrier width. These choices correspond to (d) a short QPC with a flat potential top ( $\tilde{V}_c = \tilde{V}_s$ ); (e) a QPC described by a parabolic potential top ( $\tilde{V}_c > \tilde{V}_s$ ); (f) a long QPC with a flat potential top ( $\tilde{V}_c = \tilde{V}_s$ ); and (g) a QD ( $\tilde{V}_c < \tilde{V}_s$ ).

We use the multigate layout shown in Fig. 1(a) to lat-

erally define a nanostructure in the two-dimensional electron system (2DES) located 85 nm beneath the surface of our GaAs/AlGaAs heterostructure. The low temperature charge carrier density is  $1.9 \times 10^{11} \text{ cm}^{-2}$  and the mobility  $1.2 \times 10^6 \text{ cm}^2/\text{Vs}$ . Magnetic fields are aligned parallel to the 2DES and to the 1D channel defining the QPC (current direction). The field's alignment is optimized by use of a two-axis magnet and controlled by magnetotransport measurements. The electron temperature in all measurements presented here is  $T_0 \simeq 30 \text{ mK}$  according to our estimations from separate temperature dependent measurements (not shown, see also Ref. 14).

Seven gates provide a particularly high tunability of the central constriction region (CCR) of our device, located at the center of Fig. 1(a) between the tips of six gates. We apply one voltage, say  $V_c$ , to both central gates, and another, say  $V_s$ , to all four side gates. Our sample also contains a global top gate [see Fig. 1(a),(b)], electrically insulated from other gates by a layer of cross-linked PMMA (plexiglass). The top gate can be used to adjust the carrier density of the 2DES in the contacts of the CCR and thereby control the effective interaction strength between electrons<sup>14</sup>. In this article we keep  $V_t$  fixed at 0.8 V. By suitably tuning  $V_c$  and  $V_s$ , we are able to smoothly reshape the potential landscape in the 2DES in such a way that it crosses over from a saddle point potential defining a QPC [Fig. 1(b)] to a symmetric local minimum defining a QD [Fig. 1(c)]. The corresponding effective 1D potential barrier shape crosses over from a single barrier [Figs. 1(d-f)], whose top is parabolic only in a relative narrow range of gate voltages, to a symmetric double barrier [Fig. 1(g)].

Experimentally we have studied this smooth transition from a QD to a QPC by measuring the two-terminal differential conductance  $g$  via the linear response of the current to small modulations of the applied source-drain voltage. Fig. 2 shows raw data (albeit already corrected for the lead resistances) measured at  $B = 0$  as a function of  $V_c$  and  $V_s$ . For our most negative  $V_s$ -values and near pinch-off, i. e. also negative  $V_c$ , the conductance traces show pronounced Coulomb blockade oscillations as function of  $V_c$  (at the bottom center part of the figure). This indicates that the CCR constitutes a single, well-defined QD with a substantial Coulomb charging energy. When  $V_s$  is made less negative the Coulomb blockade oscillations disappear altogether. The reason is that the local electrostatic potential near the side gates decreases and eventually becomes smaller than the electrostatic potential between the center gates, corresponding to a transition from a double barrier potential as in Fig. 1(g) to a single barrier top as in Figs. 1(d-f). In the process the QD disappears, and with it the localized states, and a clean QPC remains. Its barrier top may or may not be parabolic, depending on the value of  $V_s$ . At  $V_s \simeq -0.4 \text{ V}$ ,  $g(V_c)$  clearly shows several smooth conductance steps as function of  $V_c$ , as expected for the pinch-off curves of a clean parabolic QPC.

The broad transition regime between QPC and QD



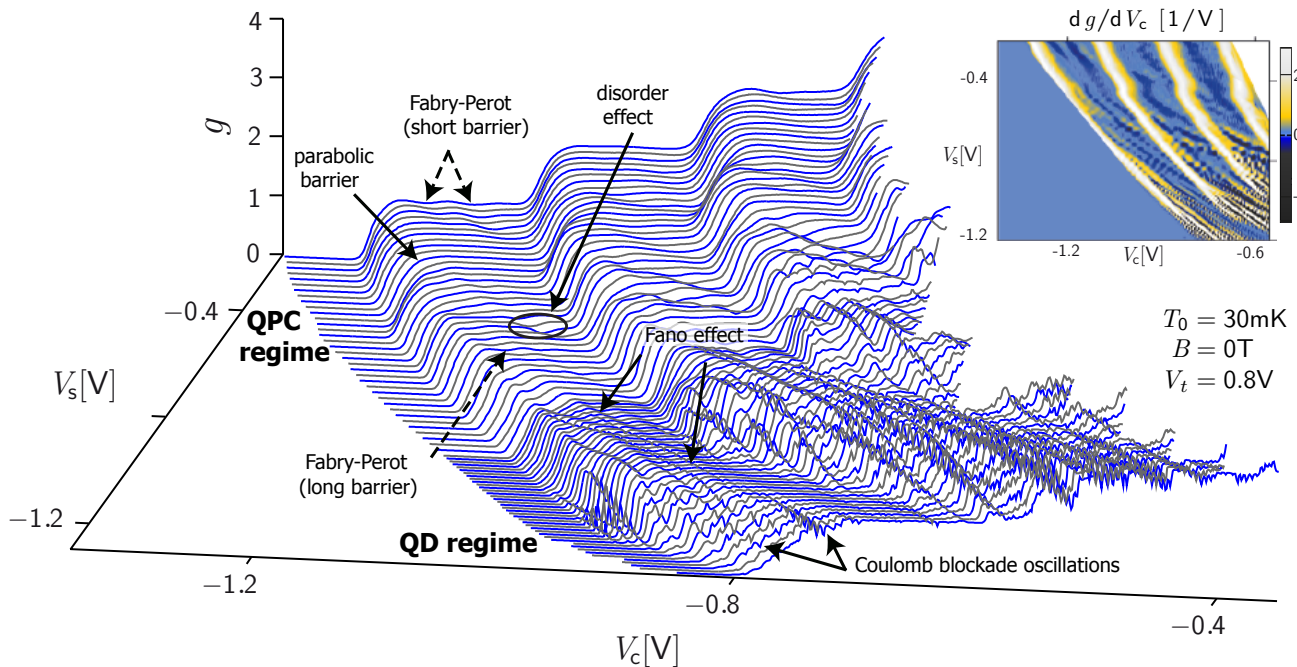


Figure 2. The linear-response differential conductance  $g$  (main panel) and transconductance  $dg/dV_c$  (inset) as a function of  $V_c$  and  $V_s$ , showing the geometric crossover between a QD and a QPC. Detailed measurements of the 0.7-anomaly at fixed side gate voltage, reported in Ref. 14 and shown in part in Fig. 6(d) below, were performed at  $V_s = -0.4$  V, where the first plateau is absolutely flat, implying a parabolic barrier top. Features marked by arrows are explained in the main text.

displays a combination of both 1D conductance steps and Coulomb blockade oscillations. The latter are most pronounced at the steps between conductance plateaus ( $0 < g < 1$ ,  $1 < g < 2$ , ...) and occur in clusters with a rather similar structure, as can be best seen in the inset of Fig. 2, which shows  $dg/dV_c$  using a color scale. This repeating pattern of Coulomb blockade oscillations indicates a coexistence of a QD in the not yet (fully) occupied one-dimensional subband of the CCR with already fully occupied lower one-dimensional subbands contributing to QPC-behavior. This causes the charge configurations of the QD to repeat at adjacent QPC conductance steps when the number of occupied one-dimensional subbands changes by one. Note that as  $V_s$  becomes more negative, the spacing between Coulomb blockade peaks within each cluster tends to increase (causing the cluster to “fan out”, see Fig. 2, inset, bottom right corner). This reflects an increase in the QD charging energy, brought about by the steepening of the confinement potential when its side barriers become higher.

Whenever a Coulomb blockade oscillation enters a conductance plateau at  $g = 1, 2, \dots$  the corresponding conductance maxima of the QD turn into narrow conductance dips, some of which are marked by solid arrows in Fig. 2. We interpret these dips as Fano resonances between the 1D channel of the QPC and localized states of the QD.

We also observe broader and very shallow conductance oscillations on the conductance plateaus deeper in

the QPC regime (at larger  $V_s$ ), marked by dashed arrows in Fig. 2. They are absent only in a narrow region around  $V_s \simeq -0.4$  V (on the first plateau), and the oscillation period observed for  $V_s < -0.4$  V is shorter than that observed for  $V_s > -0.4$  V. We interpret these as Fabry-Perot-like resonances that arise whenever the barrier shape is not parabolic: as  $V_s$  is increased within the regime of a clean QPC, starting from around  $V_s \simeq -0.8$  V, we observe a transition from a long flat barrier via a parabolic barrier near  $V_s \simeq -0.4$  V to a short flat barrier for  $V_s > -0.4$  V, where also  $V_s \gg V_c$ , (as sketched in Figs. 1(d-f) and indicated in Fig. 2). We will discuss the origin and behavior of these Fabry-Perot resonances in more detail in sections III B and III C below.

At a particular side gate voltage, near  $V_s \simeq -0.6$  V, two conductance traces show a marked dip (indicated by an ellipse) near the end of the first plateau. We interpret this distinct reduction of the conduction as reflection of electrons caused by disorder in the form of a distinct defect.

The multi-gate tunability of our device has the important advantage that it allows these type of effects (Fabry-Perot and/or disorder) to be avoided, if desired. Indeed, at side gate voltages near  $V_s \simeq -0.4$  V, no such effects are seen around the first conductance plateau is completely flat. We have therefore used  $V_s = -0.4$  V for the detailed measurements of the 0.7-anomaly reported in Ref. 14, some of which are also shown in Fig. 6(d) below. An additional option would be to apply various

different voltages to the individual four side gates or the two central gates to overcome possible disorder effects. However, the high quality of our sample rendered such options unnecessary, allowing us to maintain a high degree of symmetry of the electrostatic potential defining the CCR.

Fig. 2 displays two additional remarkable trends: (i) the quantized plateaus in  $g(V_c)$  become wider as  $V_s$  is increased. (ii) This goes along with an increase of the step width between plateaus as is best seen in the inset of Fig. 2 (consider the width of the white-yellow bands in the upper half of the plot, the QPC regime). Trend (i) indicates that the lateral confinement becomes stronger with more positive  $V_s$ , leading to a larger characteristic energy spacing between the 1D subbands. This also implies a larger on-site exchange energy,  $U$ , between the electrons. Trend (ii) confirms our statement, above, that the width of the barrier, seen by electrons, decreases as  $V_s$  is increased, because a narrower barrier causes the step width to become wider (see the discussion in Sec. III B and Figs. 3(a-c) below). Both trends together (which further depend on the topgate voltage, see Supplementary Material in Ref. 14) provide us with an experimental toolkit to precisely measure the geometry dependence of the 0.7-anomaly. This could be used for a detailed test of the predictions of our model in Ref. 14. A study of this kind is beyond the scope of this work and left for the future.

### III. THEORETICAL MODEL

In this section we present the one-dimensional model used for our theoretical description of the QD-QPC crossover, featuring a smooth barrier and short-ranged interactions [Sec. III A]. We first illustrate its geometrical properties in the absence of interactions, by showing results for the noninteracting LDOS and noninteracting transmission [Sec. III B]. Within this noninteracting framework we explain why Fabry-Perot-type resonances occur whenever the barrier top is not parabolic [Sec. III C]. Finally, we summarize the key ingredients of the fRG approach used here to treat interaction effects [Sec. III D].

#### A. Hamiltonian

To describe the QD-QPC crossover we restrict ourselves to the lowest 1D subband of the CCR and adopt the model introduced in Ref. 14 (see its Supplementary Information, Section S-4.B, “model I”), whose notational conventions we adopt here, too. The Hamiltonian has the form

$$H = \sum_{j\sigma} \left[ E_{j\sigma} \hat{n}_{j\sigma} - \tau (d_{j+1\sigma}^\dagger d_{j\sigma} + \text{h.c.}) \right] + \sum_j U_j n_{j\uparrow} n_{j\downarrow}, \quad (1)$$

where  $\hat{n}_{j\sigma} = d_{j\sigma}^\dagger d_{j\sigma}$  counts the number of electrons with spin  $\sigma$  ( $= \pm$  for  $\uparrow, \downarrow$ ) at site  $j$ . It describes an infinite tight-binding chain with constant lattice spacing  $a = 1$  (taken as length unit), constant hopping amplitude  $\tau = 1$  (taken as energy unit), on-site interaction  $U_j$  and on-site potential energy  $E_{j\sigma} = E_j - \frac{\sigma}{2} \tilde{B}$ . Here  $E_j = \tilde{E}(ja)$  models the smooth electrostatic potential  $\tilde{E}(x)$  defined by gates, and the Zeeman energy  $\tilde{B}$  accounts for a uniform external parallel magnetic field. (We use tildes to distinguish model parameters from experimental ones, with  $\tilde{B} = |g_{\text{el}}| \mu_B B$  for the magnetic field, where  $g_{\text{el}} < 0$  for GaAs,  $\tilde{T} = k_B T$  for temperature, and  $\tilde{V}_{c,s} \propto -|e|V_{c,s}$  for the central and side gate voltages.) We neglect spin-orbit interactions and other orbital effects. We take  $U_j$  and  $E_j$  to be nonzero only within a central constriction region (CCR) of  $N = 2N' + 1$  sites around  $j = 0$ , representing the QD or QPC. The rest of the chain represents two noninteracting leads with effective mass  $m = \hbar^2 / (2\tau a^2)$  (defined as the curvature of the dispersion at the band bottom in the bulk), chemical potential  $\mu$  and bulk Fermi energy  $\varepsilon_F = 2\tau + \mu$ ; we choose  $\mu = 0$ , implying half-filled leads.  $U_j$  is set to a constant value  $U$  within the CCR for all but the outermost sites of the CCR, where it drops smoothly to zero. (For an explicit formula for  $U_j$ , see Eq. (S14) of the Supplementary Information of Ref. 14.) The shape of  $E_j$  is governed by two parameters,  $\tilde{V}_c$  and  $\tilde{V}_s$ , that respectively mimic the effects of the central and side gates in experiment.  $\tilde{V}_c < \tilde{V}_s$  defines a QD with side barrier height  $\tilde{V}_s$  w. r. t.  $\mu$  [Fig. 1(f)].  $\tilde{V}_c > \tilde{V}_s$  yields a QPC with a single central barrier [Fig. 1(d)]. Its shape near the top is chosen to be parabolic<sup>3</sup>, unless stated otherwise [Fig. 4 features non-parabolic barrier tops]. We parametrize parabolic barrier tops by

$$\tilde{E}(x) \simeq \tilde{V}_c + \varepsilon_F - \frac{m\Omega_x^2 x^2}{2\hbar^2}. \quad (2)$$

Here  $\tilde{V}_c$  is the barrier height measured w. r. t. the chemical potential, and the barrier curvature is characterized by an energy scale  $\Omega_x$ . We emphasize that by “parabolic” barrier, we mean that the quadratic  $x$ -dependence of Eq. (2) holds over an energy range of at least  $\Omega_x$  from the barrier top (i.e. up to  $x$ -values large enough that  $E(0) - E(x) \gtrsim \Omega_x$ ). Then the width of the conductance step is given by  $\Omega_x$ .

Typical choices of the potentials described by  $E_j$  are shown in Figs. 1(d-g), Figs. 3(a-f) and to some extent Fig. 4 (inset). For situations where the shape of  $E_j$  is not shown explicitly [Figs. 5(a-c), Fig. 6, Figs. 7(i-l)], it is chosen according to a formula given by Eq. (S15) of the Supplementary Information of Ref. 14, with  $j_s = 60$  and  $N' = 150$  there.

#### B. Noninteracting LDOS and transmission

To convey some intuition for the geometrical properties of this model in the absence of interactions, Fig. 3 shows

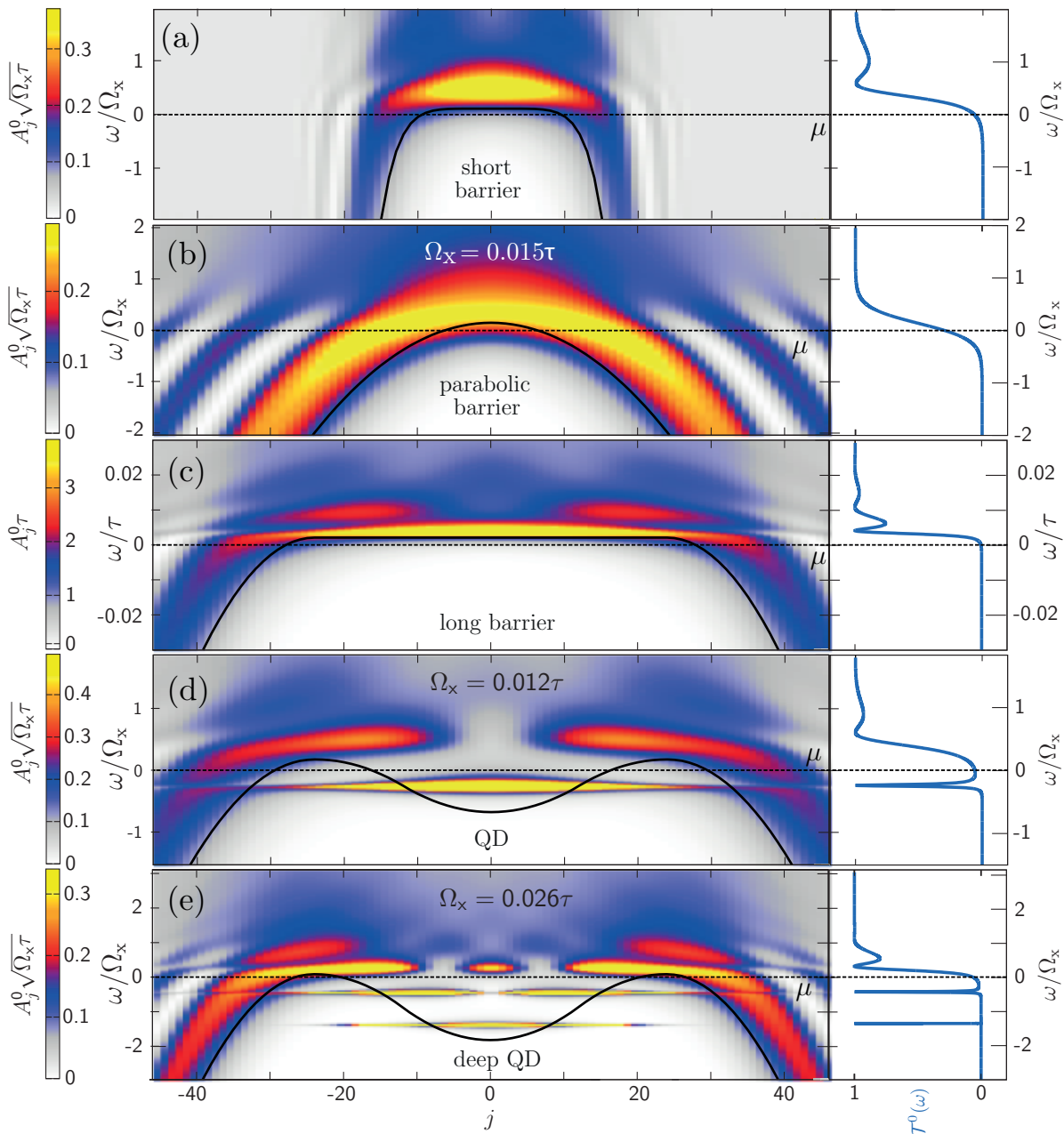


Figure 3. Noninteracting local density of states per spin species,  $\mathcal{A}_j^0(\omega)$ , and the noninteracting transmission per spin species,  $\mathcal{T}^0(\omega)$ , for  $\tilde{B} = 0$ . The energy  $\omega$  is measured w. r. t. the chemical potential. The five panels show five potential barrier shapes occurring during the QPC-QD crossover, namely (a) a QPC with a short flat barrier, (b) a QPC with a parabolic barrier, (c) a QPC with a long flat barrier, (d) a shallow QD with just one discrete orbital state, and (e) a deeper QD with two discrete orbital states.

the noninteracting LDOS,  $\mathcal{A}_j^0(\omega)$ , and the noninteracting transmission probability,  $\mathcal{T}^0(\omega)$  (with  $\omega$  measured w. r. t. the chemical potential), for five different choices of the barrier shape, chosen to represent various states of the geometric crossover between a QPC and a QD. For a parabolic QPC [Fig. 3(b)], the LDOS exhibits a broad ridge (yellow-red) just above the band bottom,  $\omega_j^{\min} = E_j - \varepsilon_F$  (solid black line), which follows the

shape of the barrier. This is the van Hove ridge mentioned in the introduction; it originates from the 1D van Hove singularity at the band bottom, which in the CCR is smeared out on a scale set by the barrier curvature  $\Omega_x$ . When  $\omega$  is increased from below to above the barrier top, set by  $\tilde{V}_c$ , the transmission  $\mathcal{T}^0(\omega)$  changes from 0 to 1 in the form of a smooth monotonic step of width  $\Omega_x$ , centered at  $\omega = \tilde{V}_c$ .

Upon raising the side gate parameter  $\tilde{V}_s$  at fixed  $\tilde{V}_c$ , the effective barrier top eventually turns flat [Fig. 3(c)] and the ridge in the LDOS narrows (while the maximal value of the LDOS above the barrier increases accordingly). This flatter-than-parabolic barrier shape causes the noninteracting transmission  $\mathcal{T}^0(\omega)$  to show wiggles at the onset of the  $\mathcal{T}^0(\omega) = 1$  plateau, which we interpret as Fabry-Perot-like resonances. They are discussed in more detail in the next subsection. Experimentally, we also observe the case of a short flat barrier for quite large  $V_s$ , which we simulate in Fig. 3(a) by using a short barrier with a quartic top (described by Eq. (3) below, with  $n = 4$ ). In agreement with the measured  $g(V_c)$  in Fig. 2 we observe Fabry-Perot-like resonances in  $\mathcal{T}^0(\omega)$  for both cases, short versus long flat barriers in panels (a) and (c), and the period of the wiggles is longer for the shorter barrier, as expected.

When the central gate parameter  $\tilde{V}_c$  is lowered below  $\tilde{V}_s$ , we enter the QD regime [Figs. 3(d) and 3(e)]. The LDOS now develops bound states, very narrow in energy, that are spatially localized inside the QD and define its single-particle spectrum. They are accompanied by resonances in the noninteracting transmission. Note, though, that the energy beyond which the  $\mathcal{T}^0(\omega) = 1$  plateau associated with full transmission sets in, is still determined by the broader LDOS ridges above the tops of the left and right barriers, which are remnants of the van Hove ridge found for the parabolic and flat barrier shapes in (b) and (a,c), respectively. This is clearly seen in the transmission curves in panels (c) and (e), which exhibit very similar Fabry-Perot-like resonances near  $\mathcal{T}^0(\omega) = 1$ . In addition,  $\mathcal{T}^0(\omega)$  in panels (d,e) shows sharp resonances at  $\omega < 0$ , reflecting the bound states in the LDOS. The occurrence of a conductance step together with sharp resonances is a clear signature of the coexistence of a QD and a QPC; our experimental data show corresponding features in the QD regime of Fig. 2.

In the outer flanks of the potential barrier, the LDOS has interference fringes with a period that scales as  $1/v$ , and the LDOS value averaged over several such fringes likewise scales as  $1/v$ , where  $v_j(\omega)$  is the semiclassical velocity of an electron with kinetic energy  $\omega - \omega_j^{\min}$  at site  $j$ . This explains the strikingly different behavior of the LDOS at the flanks of the potential maxima in Figs. 3(a) and 3(b): For the short, flat barrier with steep flanks in Fig. 3(a), the velocity  $v_j(\omega)$  of electrons with  $\omega \simeq \mu$  increases rapidly with  $|j|$ . As a consequence the LDOS at  $\mu$  decreases rapidly and forms interference fringes with an correspondingly rapidly decreasing period. For the parabolic barrier of Fig. 3(b) the flanks decrease much more slowly with increasing  $|j|$ , thus the corresponding increase in Fermi velocity, the decrease in the average LDOS and the decrease in the interference period all occur more slowly, too.

### C. Fabry-Perot resonances

In this section, we discuss the Fabry-Perot-like resonances (wiggles) that are seen in both the measured conductance in Fig. 2 (marked by dashed arrows) as well as in the calculated  $\mathcal{T}^0(\omega)$ , e.g. in Figs. 3(a,c), in more detail.

For our 1D model, studied in the absence of interactions, we find, in particular, that  $\mathcal{T}^0(\omega)$  shows Fabry-Perot-like resonances whenever the QPC barrier top is flatter than parabolic. This is illustrated in Fig. 4, which

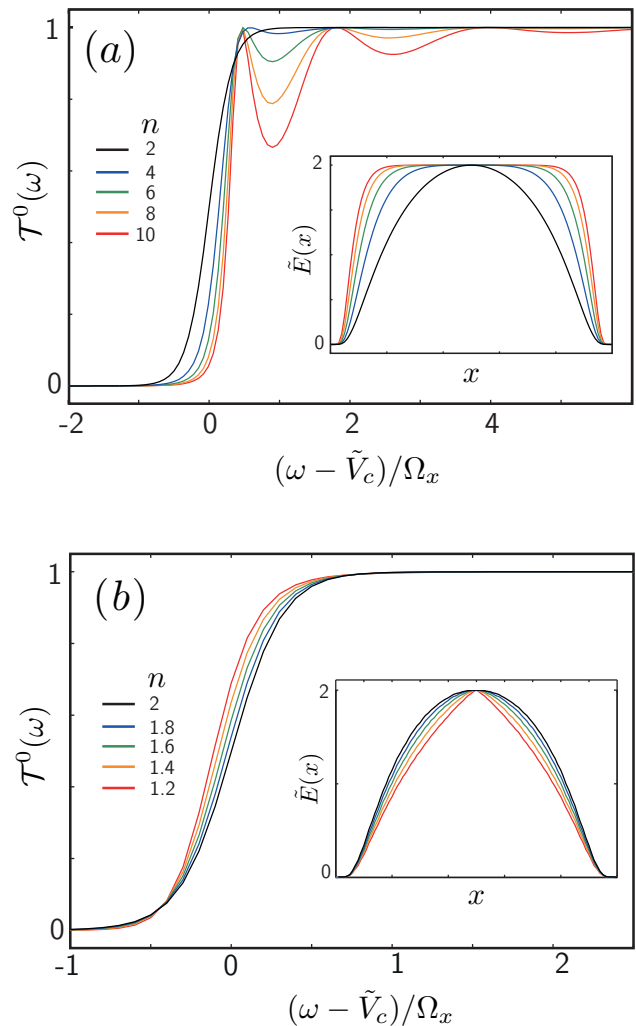


Figure 4. Noninteracting transmission  $\mathcal{T}^0(\omega)$  as function of central gate voltage for several different barrier shapes, depicted in the insets, with barrier tops governed by  $|x|^n$  according to Eq. (3). (a) Flatter-than parabolic barriers with  $n \geq 2$ , which arise during the QPC-KQD crossover; (b) sharper-than parabolic barriers with  $n \leq 2$ , shown for completeness.

shows the noninteracting conductance  $g^0(\tilde{V}_c)$  for a se-



quence of barrier shapes with barrier tops given by

$$\tilde{E}(x) = \tilde{V}_c + \varepsilon_F - \Omega_x \left( \frac{|x|}{l_x} \right)^n, \quad l_x = \sqrt{\frac{2\hbar^2}{m\Omega_x}}, \quad (3)$$

where  $l_x$  is a characteristic length. The noninteracting transmission of a purely parabolic barrier top ( $n=2$ , black line) is a smooth function of energy, given by<sup>3</sup>

$$\mathcal{T}^0(\omega) = [e^{2\pi(\tilde{V}_c - \omega)/\Omega_x} + 1]^{-1}. \quad (4)$$

In contrast, making the barrier top flatter than parabolic by increasing  $n$  introduces additional wiggles or resonances in  $\mathcal{T}^0(\omega)$ , see Fig. 4(a). Note that such structures occur naturally in the conductance of longer QPCs and we suspect that some previously published QPC measurements have likely been performed in this regime of flatter-than-parabolic barriers<sup>32,33</sup>. Our own experimental results, displayed in Fig. 2, demonstrate that the transition from a gate defined QD to a QPC likely covers the regime of a long QPC with a flatter-than-parabolic barrier top and, moreover, a short QPC with steep flanks can also result in a flatter-than-parabolic barrier and Fabry-Perot-like resonances.

For completeness, Fig. 4(b) shows examples of  $n \leq 2$ . Here, the transmission increases purely monotonically, without any Fabry-Perot-like resonances. With decreasing  $n$ , the potential flanks tend to “flatten”, causing the conductance step to develop an increasingly skewed shape: the step’s onset becomes noticeably steeper, while the onset of the plateau is affected only weakly.

We note that it is not straightforward to distinguish Fabry-Perot-type resonances, that occur even without interactions, from many-body effects, that arise in the presence of interactions. In the light of recent experimental work on shape-dependent barriers, including Refs. 32 and 33 and this work, a systematic theoretical study of how Fabry-Perot-type resonances are affected by turning on interactions would be very interesting, but is beyond the scope of this work.

#### D. fRG approach

To theoretically study the effect of interactions on the properties of the CCR at zero temperature, we used fRG<sup>28–31</sup>, a renormalization-group-enhanced perturbative expansion in the interaction. We used it to calculate the linear conductance  $g$  of the CCR, and three local quantities, the occupation  $n_j$ , magnetization  $m_j$  and spin susceptibility  $\chi_j$  of site  $j$ , defined, respectively, as

$$n_j = \langle \hat{n}_{j\uparrow} + \hat{n}_{j\downarrow} \rangle, \quad (5a)$$

$$m_j = \langle \hat{n}_{j\uparrow} - \hat{n}_{j\downarrow} \rangle / 2, \quad (5b)$$

$$\chi_j = \partial_{\tilde{B}} m_j |_{\tilde{B}=0}. \quad (5c)$$

The results are presented in Secs. IV and V, below.

The details of our fRG approach are explained concisely in the supplement of Ref. 14, and in more detail

in Ref. 31. Here we just summarize some key aspects. We restrict ourselves to zero-temperature calculations in the Matsubara formalism. Our fRG flow equations are based on two criteria. First, we assume that  $m_j = 0$  for  $\tilde{B} = 0$ , thus spontaneous symmetry breaking is ruled out *a priori*. This assumption is justified *a posteriori* by the agreement of our fRG results with experiment, both in Ref. 14 and in the present paper. Second, we neglect all contributions to the flow of the interaction vertex that are not already generated to second order in the bare (onsite) interaction, but feed back all other terms. This so-called coupled ladder approximation<sup>31</sup> amounts to including all RPA-like channels on equal footing, while feeding back all Hartree-like terms into the Fock-like equations and vice versa. As a computational simplification, we here use a “static” version of the coupled-ladder approximation, which neglects all frequency dependencies in self-energies and vertices. For the model of present interest, the results for the zero-temperature conductance obtained via this static simplification are qualitatively essentially the same as those obtained by a “dynamic” calculation in which the frequency dependence is retained, as shown explicitly in Refs. 14 and 31 for a parabolic QPC potential.

The effective expansion parameter for static fRG is  $U_j \mathcal{A}_j^0(0)$ . As a result, we find that the fRG equations describing vertex flow do not converge for geometries that cause  $\mathcal{A}_j^0(\omega)$  to be sufficiently sharply peaked near the chemical potential, i. e. near  $\omega = 0$ . This problem occurs in the QD regime, where the shallow few-electron QD has wide barriers near  $\mu$ . We have therefore neglected vertex flow for plots that involve this regime, i. e. in Figs. 5(a-c), and for the movie discussed in App. A. Vertex flow was included, however, for all other fRG results shown in this paper, and is essential for obtaining the 0.7-shoulder in the QPC conductance even at  $\tilde{B} = \tilde{T} = 0$ , as discussed in Sec. IV B below.

In Ref. 14, we showed that our model and fRG treatment of interactions are able to capture key elements of the 0.7-anomaly in a QPC in a qualitatively correct manner, including its magnetoconductance. In the next section, we show that this is true also for the Kondo effect in a KQD, and in fact for the entire QD-QPC crossover.

## IV. MAGNETOCONDUCTANCE

In this section, we compare zero-temperature fRG results and low-temperature experimental data for the conductance during geometrical QD-QPC crossover, for three different magnetic fields [Sec. IV A]. We also discuss the magnetoconductance in the KQD and QPC regimes in more detail, showing that fRG reproduces the characteristic magnetic-field dependence associated with the Kondo effect and the 0.7-anomaly, respectively [Sec. IV B]. Moreover, we discuss the  $\tilde{V}_c$ -dependence of the characteristic low-energy scale,  $\tilde{B}_*$ , that characterizes the strength of the magnetoconductance at low fields,



and its relation to the static spin susceptibility of the CCR [Sec. IV C].

### A. QPC-QD crossover at finite magnetic field

Fig. 5 compares fRG results and experimental data for the QD-QPC crossover at three magnetic fields, including the  $B = 0$  data already shown in Fig. 2. Figs. 5(a-c) present model calculations of the zero-temperature linear conductance  $g(\tilde{V}_c, \tilde{V}_s)$  (using fRG without vertex flow) for three magnetic field values, and Figs. 5(d-f) corresponding experimental data. The pinch-off value of  $V_c$  around which the measured conductance drops to zero as  $V_c$  is decreased, say  $V_c^{\text{pinch}}$ , is indicated using red lines in the raw data for  $B = 0$  in Figs. 5(h,i), which are miniature versions of Fig. 2 and its inset. Note that  $V_c^{\text{pinch}}$  shifts as a function of  $V_s$ , reflecting the capacitive influence of  $V_s$  on the local potential between the center gates. This effect is absent in the calculated data, since our model does not include such a cross-coupling. For better comparison between theory and experiment, this cross-coupling is corrected for in the measured data in Figs. 5(d-f), by plotting them as function of  $\Delta V_c = V_c - V_c^{\text{pinch}}$ .

The measured transition from a QD to a QPC in Figs. 5(d-f) is smooth regardless of  $B$ . Our calculations qualitatively reproduce the main features of the measured QPC-QD crossover: Just as for the  $B = 0$  data in Fig. 2, both the calculated and measured conductance traces in Figs. 5(a-f) show the transition between a single QD with Coulomb blockade oscillations and a QPC with a smooth conductance step. A movie showing how this crossover evolves continuously with magnetic field is presented and discussed in App. A.

Moreover, both the calculated (at  $T = 0$ ) and measured (at  $T_0 \simeq 30$  mK) data exhibit the Kondo effect in the QD regime: it manifests itself as an enhanced conductance in the Coulomb blockade regime if an odd number of electrons charges the QD. In such Kondo valleys, highlighted in Figs. 5(a-f) by red lines, the Kondo-enhanced conductance is strongly suppressed with increasing field. Fig. 5(g) illustrates this for the measured data by showing in a single panel the three colored pinch-off curves from Figs. 5(d-f), taken for three comparable values of side gate voltage  $V_s$ . (These three values,  $V_s = -1.18, -1.14$  and  $-1.18$ , are not all the same, because a random charge fluctuation had occurred in the sample between the respective measurement runs, shifting the potential landscape by a small but noticeable amount.) The solid red arrows in Fig. 5(g) mark the two Kondo valleys corresponding to the red lines in Figs. 5(d-f). The dashed red arrow in Fig. 5(g) marks a third Kondo valley at a smaller  $V_c$ -value, where, however, the Kondo effect is already very weak, since the coupling to the leads is so small that  $T_K < T$ .

In the regime of a QPC defined by a parabolic barrier (small  $\tilde{V}_s$ , large  $V_s$ ), both measurements and calculations display the typical magnetic field dependence of the 0.7-

anomaly [marked by orange lines in Figs. 5(a-f)], namely the development from a weak shoulder at  $g \simeq 0.7$  for  $B = 0$  to a pronounced plateau at a reduced conductance for finite magnetic fields.

### B. Magnetoconductance of QPC and KQD

In this subsection we compare theory and experiment in more detail, for the magnetoconductance at two fixed values of side gate voltage, for which the system forms a KQD or a QPC, respectively. For the QPC, we have tuned the experimental system to have a smooth plateau at  $g = 1$  without any Fabry-Perot resonances on the first conductance plateau ( $V_s = -0.4$  V, compare Fig. 2), while we use a parabolic barrier top for the theoretical calculations.

Figs. 6(a,b) show measured conductance of a KQD and a QPC, respectively, at several magnetic fields,  $0 \leq B \leq 5.8$  T, and Figs. 6(c,d) show corresponding fRG results (calculated with flowing vertex). The fRG calculations qualitatively reproduce the gate voltage and field dependencies observed by us and numerous other experimental groups: The conductance of the KQD [Fig. 6(c)] shows a Kondo plateau for  $\tilde{B} = 0$ , which is suppressed into a dip with increasing field, as expected theoretically<sup>29,34</sup> and observed experimentally in Ref. 20 and for our own data [Fig. 5(g), Fig. 6(a)]. The conductance step of the QPC [Fig. 6(d)] exhibits a 0.7-shoulder at  $\tilde{B} = 0$ , which, as  $\tilde{B}$  is increased, is suppressed into a double step whose width is proportional to the magnetic field, as also seen in numerous experiments<sup>4,7,9</sup>, including our own (Fig. 6(b), see also Ref. 14).

Note that the shoulder at  $g \simeq 0.7$  is visible in Fig. 6(d) even for  $B = 0$ , much more so than in Fig. 5(a) above; the reason is that the fRG scheme without vertex flow used for Figs. 5(a-c) underestimates the effects of interactions compared to the fRG scheme that includes vertex flow, used for Figs. 6(c,d). For a detailed discussion of this point, see Ref. 14.

### C. Low-energy scale and excess spin susceptibility

For both KQD and QPC, the low-field expansion of  $g$ ,

$$g(\tilde{B}) \simeq g(0)[1 - (\tilde{B}/\tilde{B}_*)^2] \quad (\tilde{B} \ll \tilde{B}_*), \quad (6)$$

can be used to characterize the strength of the  $\tilde{B}$ -dependence in terms of a  $\tilde{V}_c$ -dependent energy scale,  $\tilde{B}_*$ : the smaller  $\tilde{B}_*$ , the larger the magnetoconductance. For KQDs, the scale  $\tilde{B}_*$  in Eq. (6) corresponds to the Kondo temperature,  $\tilde{B}_*^{\text{KQD}} = k_B T_K$ , according to Nozières' Fermi-liquid<sup>26,35</sup> description of the low-energy limit of the Kondo model. The  $\tilde{B}^2$ -dependence (6) has recently been observed experimentally for a KQD<sup>22</sup> and previously for a few electron double quantum dot<sup>36</sup>; for a

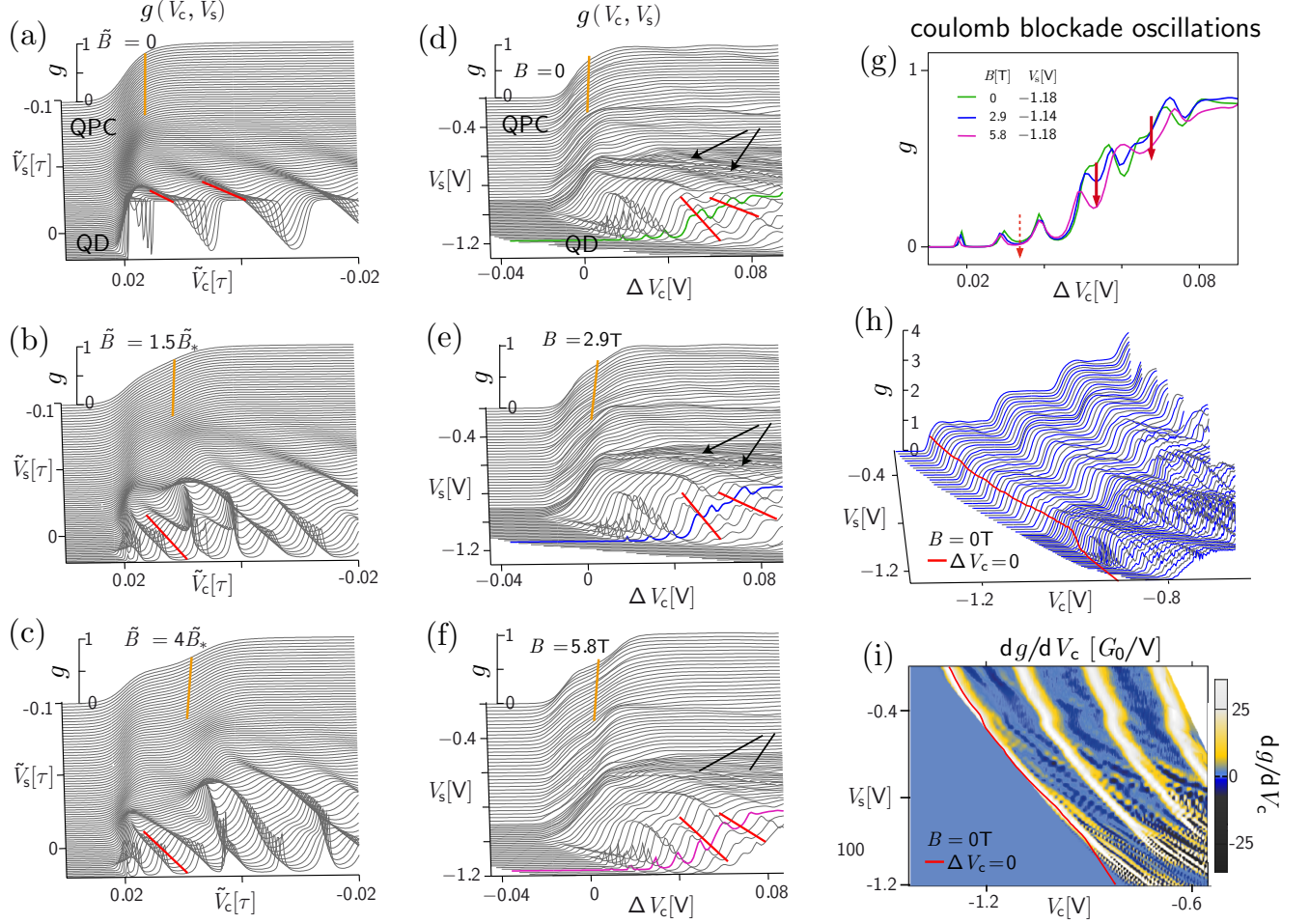
fRG ( $T=0, U=0.5\tau, \tilde{B}_* = 10^{-3}\tau$ )Experiment ( $T_0 = 30\text{mK}, V_t = 0.8\text{V}$ )

Figure 5. Transition from a QD to a QPC. (a-c) fRG1 results for the conductance  $g(\tilde{V}_c, \tilde{V}_s)$ , calculated at  $T = 0$  and three different fields, and plotted as function of the central gate voltage  $\tilde{V}_c$  for a large number of different side gate voltages  $\tilde{V}_s$ . (d-f) Analogous to (a-c), but showing experimental data for the conductance  $g(V_c, V_s)$  in the range  $0 \leq g \leq 1$ , measured at a fixed low temperature,  $T_0 = 30\text{ mK}$ . For each side gate voltage  $V_s$ , the conductance trace is plotted as function of the shift  $\Delta V_c = V_c - V_c^{\text{pinch}}$  in central gate voltage  $V_c$  relative to a  $V_s$ -dependent reference value  $V_c^{\text{pinch}}(V_s)$ , which is indicated by red lines in panels (h) and (i). [We chose  $V_c^{\text{pinch}}$  to satisfy  $g(V_c^{\text{pinch}}) = 0.5$  in the QPC regime ( $V_s > -1\tilde{V}$ ), and to shift linearly with  $V_s$  in QD regime, with a slope chosen such that the red line does not cross any resonances.] Orange lines in (a-f) mark the 0.7-anomaly, red lines mark Kondo valleys; black arrows in (d-f) mark Fano resonances. (g) The three colored pinch-off curves from (d-f), all measured at  $V_s = -1.18\text{ V}$ , are plotted together to show how in Kondo valleys (marked by red arrows) the Kondo-enhanced conductance is suppressed by increasing field. (h) The raw experimental data for  $g(V_c, V_s)$  at  $B = 0$  [corresponding to (d)] is plotted over a larger range of (unshifted) gate voltages to show several conductance steps. (i) The derivative  $dg/dV_c$  of the data from panel (h). [(h) and (i) show identical data as Fig. 2 and its inset.] The red lines in (h) and (i) show  $V_c^{\text{pinch}}(V_s)$ , as used in (d-f).

QPC, it has been confirmed in Ref. 14 Fig. 2g there). Extracting  $\tilde{B}_*(V_c)$  from our fRG results (Figs. 6(e,f), red lines) we find that for both KQD and QPC it exhibits a distinct minimum,  $\tilde{B}_*^{\text{min}}$ , at (say)  $\tilde{V}_{c0}$ , near which it

behaves as

$$\tilde{B}_*^{\text{KQD}} \propto \exp[c_1(\tilde{V}_{c0} - \tilde{V}_c)^2], \quad (7a)$$

$$\tilde{B}_*^{\text{QPC}} \propto \exp[c_2(\tilde{V}_{c0} - \tilde{V}_c)/\Omega_x], \quad (\tilde{V}_c < \tilde{V}_{c0}), \quad (7b)$$

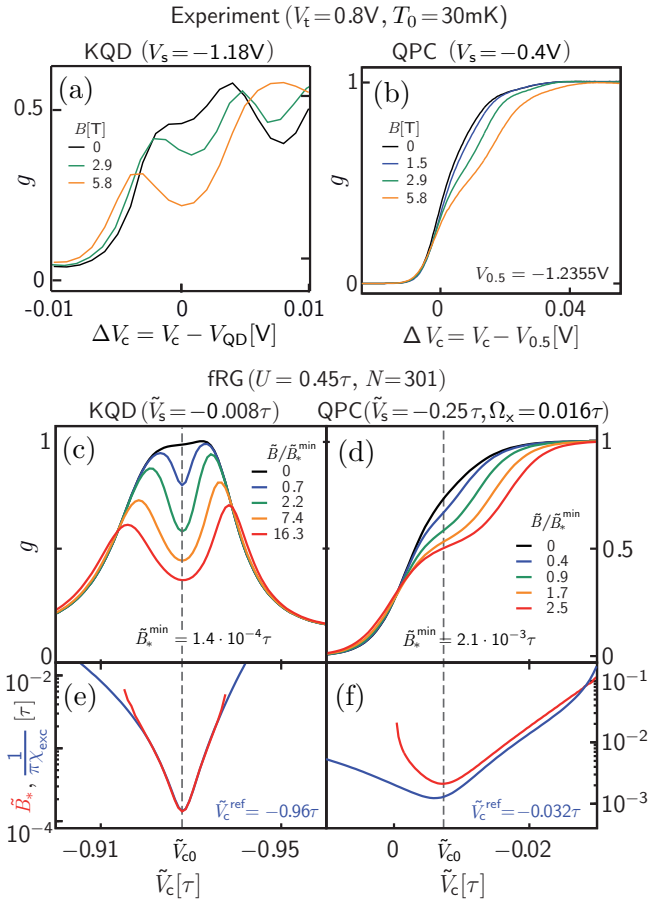


Figure 6. Magnetoconductance: experiment vs. theory. (a,b) Experimental conductance curves for a KQD and a QPC, at two different, fixed  $V_s$ -values and various magnetic fields measured at a low temperature  $T_0 = 30$  mK. Here,  $\Delta V_c$  is the offset of the central gate voltage  $V_c$  relative to  $V_{\text{QD}}$  or  $V_{0.5}$ , denoting the middle of the Kondo valley or the middle of the first conductance step, respectively. The data in (a) are a subsection of those shown in Fig. 5(g); the data in (b) correspond to those shown in Ref. 14, Fig. 2e. (c,d) fRG results, plotted in a way analogous to (a,b), for the conductance  $g(\tilde{V}_c, \tilde{B})$  at fixed  $\tilde{V}_s$  of a (deep) KQD containing  $n^{\text{KQD}} = 49$  electrons, or for the lowest subband of a QPC, respectively. (e,f) The corresponding KQD and QPC low-energy scales  $\tilde{B}_*(\tilde{V}_c)$  [red lines, from Eq. (6)] and inverse excess spin susceptibilities  $1/[\pi\chi_{\text{exc}}(\tilde{V}_c)]$  [blue lines, from Eq. (9)], plotted on a log-linear scale. Note that near the gate voltage  $\tilde{V}_{c0}$  [dashed line] where  $\tilde{B}_*$  reaches its minimum,  $\tilde{B}_*^{\text{min}}$ , the small-field magnetoresponse in (c,d) is strongest.

for the KQD and QPC geometries, respectively. ( $c_1$  and  $c_2$  are  $\tilde{V}_c$ -independent constants.) Eq. (7a) reproduces for  $\tilde{B}_*$  the behavior theoretically predicted<sup>27</sup> and experimentally observed<sup>19,22</sup> for the Kondo temperature of a KQD. The linear exponential behavior described by Eq. (7b) for a QPC is valid even in the absence of interactions. There it follows directly from the non-interacting transmission formula for parabolic barriers, Eq. (4) (see Sec. S-5 of

Ref. 14). Experimentally, Eq. (7b) has been confirmed in Ref. 14 (Fig. 2e there). Thus, our 1D model and fRG treatment of interactions correctly capture the full  $B$ - and  $V_c$ -dependence of the conductance of both KQD and QPC, including the exponential dependence of  $B_*$  on  $\tilde{V}_c^2$  or  $\tilde{V}_c$ , respectively.

For the Kondo effect, the scale  $\tilde{B}_*$  defined by Eq. (6) is inversely proportional to the excess contribution of the KQD to the static spin susceptibility at zero temperature,

$$1/\tilde{B}_*^{\text{KQD}} = \pi\chi_{\text{exc}}. \quad (8)$$

This relation, which links the strength of the magnetoconductance to that of local spin fluctuations, is a hallmark of Nozières's Fermi-liquid theory.<sup>26</sup> For our model, we define the excess spin susceptibility of the CCR by

$$\chi_{\text{exc}}(\tilde{V}_c) = \sum_{j \in \text{CCR}} [\chi_j(\tilde{V}_c) - \chi_j(\tilde{V}_c^{\text{ref}})], \quad (9)$$

where  $\chi_j$  [Eq. (5c)] is the local zero-field spin susceptibility of site  $j$ , and  $\tilde{V}_c^{\text{ref}}$  a reference potential at which the magnetoconductance is very small. As reference for a KQD, we take  $\tilde{V}_c^{\text{ref}}$  to define an even QD (EQD) charged by an even number of electrons in an adjacent Coulomb-blockade valley; for a QPC, we take  $\tilde{V}_c^{\text{ref}}$  small enough to define a truly open 1D channel ( $g > 0.999$ ). We find that the characteristic Fermi-liquid relation

$$1/\tilde{B}_* \propto \chi_{\text{exc}} \quad (10)$$

is satisfied very well for the KQD for  $\tilde{V}_c$  near  $\tilde{V}_{c0}$  [Fig. 6(e)], as expected. Remarkably, we find that for a QPC, too, a small  $\tilde{B}_*$  goes hand in hand with a large  $\chi_{\text{exc}}$ . In fact, by using  $\tilde{V}_c^{\text{ref}}$  as fit parameter, the inverse proportionality Eq. (10) can be achieved for a QPC over a rather large range of gate voltages  $\tilde{V}_c \lesssim \tilde{V}_{c0}$ , as shown in Fig. 6(f). That the inverse relation between  $\tilde{B}_*$  and  $\chi_{\text{exc}}$  also holds roughly for a QPC (though not as well as for a KQD, and requiring a fit parameter in the definition of  $\chi_{\text{exc}}$ ) is truly remarkable and constitutes one of the main theoretical results of this paper: the link between the *magnetoconductance* and *local spin fluctuations* that characterizes the Fermi-liquid regime of the Kondo effect, namely Eq. (10), applies for the 0.7-anomaly as well. This substantiates the argumentation, presented by us in Ref. 14, that the .7KS is a manifestation of the fact that a KQD and a parabolic QPC show similar Fermi-liquid behavior at low energies.

Below, we further explore this link by theoretically studying the relation between the magnetoconductance and local properties in more detail, and for several different QD-QPC crossover trajectories.

## V. LOCAL PROPERTIES

In this section we study the local properties of the CCR at zero temperature, calculated by fRG. We here focus



on the local density  $n_j$ , magnetization  $m_j$  and spin susceptibility  $\chi_j$  [defined in Eq. (5) above]. We find that a strong negative magnetoconductance goes hand in hand with an enhanced local spin susceptibility in the CCR, and argue that this connection is the microscopic origin of the .7KS.

Figs. 7(c-f) compare the  $\tilde{B}$ -dependence of  $n_j$  and  $m_j$  of a KQD and a parabolic QPC near pinchoff, whose barrier shapes are shown by solid lines in Figs. 7(a,b), respectively. Towards the edges of the CCR (large  $|j|$ ,  $E_j \rightarrow 0$ ), the density  $n_j$ , plotted in Figs. 7(c,d), rises toward the filling of the non-interacting leads. For the KQD the charge near the center of the CCR is well-localized and discrete [ $n_j^{\text{KQD}}$  sums to  $n^{\text{KQD}} = 9$  between the two distinct minima in (c)]. For the parabolic QPC, in contrast,  $n_j^{\text{QPC}}$  is minimal at the center, showing no signs of localized charge. For  $\tilde{B} \neq 0$ , both  $m_j^{\text{KQD}}$  and  $m_j^{\text{QPC}}$ , plotted in Figs. 7(e,f), show strongly-enhanced standing-wave oscillations in the CCR (with locally varying wavelength  $\lambda \sim 1/n_j$ ), but significant differences arise when  $\tilde{B}$  increases far beyond  $\tilde{B}_*$ : For a KQD,  $m_j^{\text{KQD}}$  saturates in magnitude, its maxima stay fixed in position, and  $n_j^{\text{KQD}}$  remains  $\tilde{B}$ -independent, all indicating that a discrete spin is being polarized. In contrast, for a QPC,  $m_j^{\text{QPC}}$  does not saturate for  $\tilde{B} \gg \tilde{B}_*$ , its maxima shift outward, and  $n_j^{\text{QPC}}$  increases near the barrier center, all indicating that a smooth redistribution of charge and spin occurs during the polarization of the CCR, which ultimately causes the spin-split double conductance step at  $\tilde{B} \gg \tilde{B}_*$ . We conclude that whereas the KQD harbors a discrete, localized spin- $\frac{1}{2}$  local moment, a parabolic QPC does not, since the spins in its CCR are neither discrete nor localized. A detailed study of the behavior of the magnetization in large fields  $B > B_*$  follows in the next section below.

Despite these differences, the KQD and QPC do show two striking similarities in the regime of small fields,  $\tilde{B} \ll \tilde{B}_*$ , relevant for the .7KS. First,  $m_j$  vanishes at  $\tilde{B} = 0$  (Figs. 7(e,f), blue lines), reflecting our fRG assumption that no spontaneous magnetization occurs, in contrast to the spontaneous spin splitting scenario advocated in Refs. 4–6, and 13 (see Ref. 14, Supplementary Information, p. 5 and 6, for a detailed discussion). Second, the local static spin susceptibility  $\chi_j$ , shown in Figs. 7(g,h), exhibits a *strong enhancement* (modulated by standing-wave oscillations) in the CCR for *both KQD and QPC*. This enhancement arises through an interplay of geometry and interactions. In the absence of interactions, the bare local spin susceptibility in a QPC is directly proportional to the LDOS at the chemical potential,  $\chi_j^0 = \mathcal{A}_j^0(0)/2$ , and hence inherits the spatial dependence of the latter, reflecting the geometry of the system. Interactions enhance the spin susceptibility via a Stoner-type mechanism: upon turning on a small Zeeman field that favors spin up over spin down, interactions enhance the spin imbalance by further depleting the spin-down population. The same line of arguments applies for a

KQD in the low-energy regime described by an effective Fermi-liquid Hamiltonian, involving quasi-particles that experience a local interaction whose strength is proportional to  $1/T_K$ <sup>26</sup>.

In contrast to a KQD, an EQD shows no  $\chi_j$ -enhancement. This is illustrated by Figs. 7(i-l), which display  $\chi_j(\tilde{V}_c)$  and  $g(\tilde{V}_c)$  for four trajectories in the  $(\tilde{V}_c, \tilde{V}_s)$  plane, corresponding to four types of geometric crossovers. Fig. 7(i) shows a QD at fixed  $\tilde{V}_s$ , whose electron number (blue integers) is increased by lowering  $\tilde{V}_c$ . It exhibits odd-even effects for both  $\chi_j(\tilde{V}_c)$  and  $g(\tilde{V}_c)$ : the Kondo-plateaus in  $g(\tilde{V}_c)$  for odd electron numbers (KQDs) are accompanied by distinct peaks in  $\chi_j(\tilde{V}_c)$  (white lines) whereas the Coulomb valleys for even electron numbers (EQDs) are not. Fig. 7(j) shows a QPC at fixed  $\tilde{V}_s$ , which is tuned from pinchoff into an open channel with  $g = 1$  by lowering  $\tilde{V}_c$ . The 0.7-anomaly in  $g(\tilde{V}_c)$  occurs for  $\tilde{V}_c$  values near  $\tilde{V}_{c0}$  (red dashed line) where  $\tilde{B}_*$  is minimal. There the two maxima in  $\chi_j$  merge into a single one (reminiscent of Figs. 2bA-C in Ref.<sup>25</sup>), indicating that the barrier top has dropped below 0 (compare panel Fig. 7(b), green circle), so that the chemical potential cuts through the apex of the Hove ridge. Fig. 7(k) shows a QPC-KQD crossover ending in an 11-electron KQD:  $\chi_j$  exhibits strong maxima in the QPC, which weaken in the open-channel regime during the crossover to the KQD, where they become large again. Fig. 7(l) shows a QPC-EQD crossover ending in a 10-electron EQD, where  $\chi_j$  remains very small, in contrast to the case of the 11-electron KQD in Fig. 7(k). Note that in the QPC parts of Figs. 7(j-l),  $\chi_j$  exhibits a ridge-like, parabola-shaped main maximum as function of  $\tilde{V}_c$  and  $j$  that mimicks (and indeed stems from) the Hove ridge in the LDOS as function of  $\omega$  and  $j$  [Fig. 3(a)].

The main message of Figs. 7(i-l) is that the *negative magnetoconductance* seen for both KQDs and QPCs, but not for EQDs, goes hand in hand with a *strongly enhanced spin susceptibility*, whereas the latter vanishes or is weak for EQDs and open 1D channels. This is direct microscopic evidence that the strong negative magnetoconductance observed in both a KQD and a QPC as one of the key features of the .7KS, originates from the fact that *a QPC harbors strong local spin fluctuations* similar to those of a KQD. In this regard, our scenario is fully consistent with the quasi-bound state Kondo scenario proposed by Meir and collaborators<sup>23–25</sup>. In fact, the spatial structure of  $\chi_j^{\text{QPC}}$  seen in Figs. 7(j-l), namely two peaks that merge into one as  $\tilde{V}_c$  is lowered, is consistent with that of the spin density of the “quasi-bound states” found for a QPC by SDFT calculations<sup>25,37</sup> (Figs. 2bA-C in Ref. 25). This is not surprising, since the SDFT calculations were initialized using a small magnetic field to break spin symmetry, which naturally gives rise to spin density maxima in regions of large spin susceptibility.

We emphasize, though, that the .7KS applies only for low energy scales,  $\tilde{B} \ll \tilde{B}_*$ , because while a KQD har-



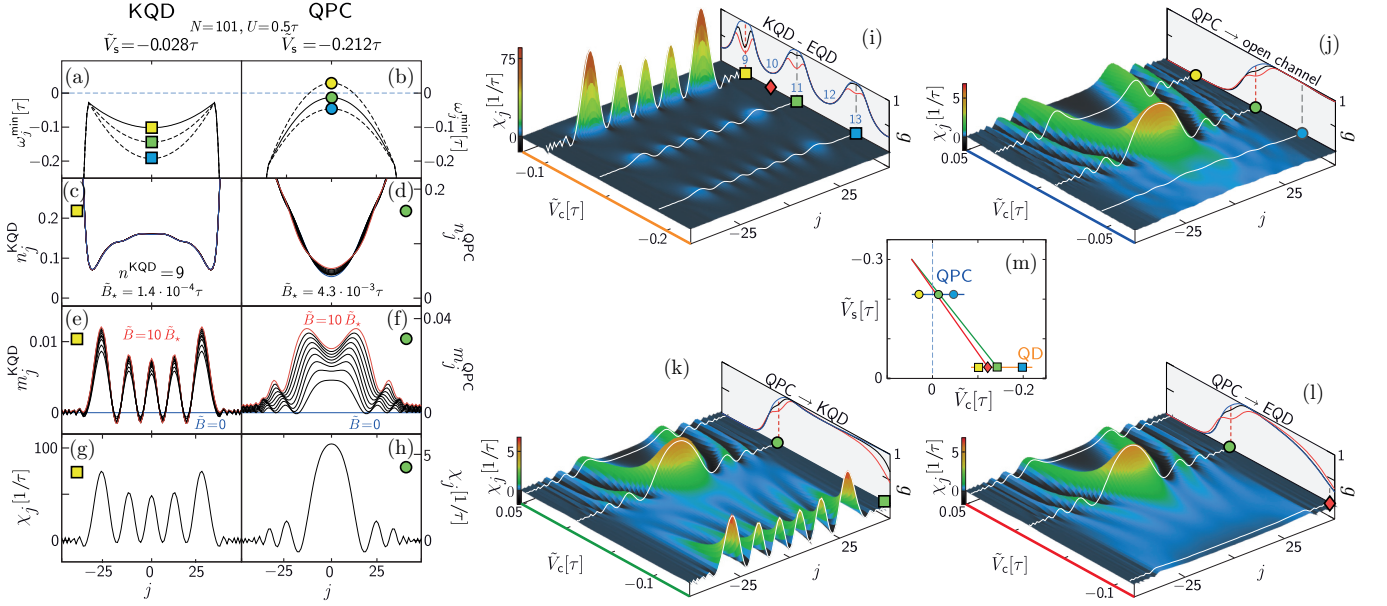


Figure 7. Local properties of KQD [charged with  $n^{\text{KQD}} = 9$  electrons for (c,e,g)] vs. QPC, calculated using fRG including vertex flow. (a-f) *Fixed geometries of KQD (left) and QPC (right)*: (a,b) The barrier tops for a (shallow) KQD and a QPC near pinchoff, respectively; for each, we show three barrier shapes  $\omega_j^{\text{min}} = E_j - \varepsilon_F$ , used to calculate the curves in (c-l) marked by matching colored symbols. (c,d) Local density  $n_j$ , and (e,f) local magnetization  $m_j$ , for 11 equidistant fields from  $\tilde{B} = 0$  (blue) to  $\tilde{B} = 10\tilde{B}_*$  (red), for the KQD and QPC potentials shown by solid lines in (a,b), respectively. (g,h) The local spin susceptibility  $\chi_j$  for the KQD and QPC potentials shown by solid lines in (a),(b), respectively; the spatial structure of  $\chi_j$  reflects that of  $m_j$  for small fields, likewise showing strongly-enhanced standing-wave oscillations in the CCR. (i-l) *Geometric crossovers*:  $\chi_j$  is shown as a function of site  $j$  and  $\tilde{V}_c = \tilde{V}_{j=0}$  for four trajectories in the  $(\tilde{V}_c, \tilde{V}_s)$  plane, drawn color-coded in panel (m) [where colored symbols mark  $\tilde{V}_c$ - and  $\tilde{V}_s$ -values used in (a-l)]. Each panel (i-l) also shows  $g(\tilde{V}_c)$  for three fields ( $\tilde{B}/\tilde{B}_*^{\text{min}} = 0, \sim 1, \text{ and } \gg 1$ ), to indicate the  $\tilde{V}_c$ -dependence of the magnetoconductance; red dashed lines mark the gate voltage,  $\tilde{V}_{c0}$ , where  $\tilde{B}_*$  takes its minimal value,  $\tilde{B}_*^{\text{min}}$ . (i) A QD being charged starting from 9 electrons (up left) to 13 electrons (down right), showing Coulomb blockade oscillations, (j) a QPC tuned from pinchoff to an open channel, (k) a crossover from a QPC to a KQD with 11 electrons, and (l) a crossover from a QPC to an even QD (EQD) charged by 10 electrons.

bors a discrete, localized spin- $\frac{1}{2}$  local moment, a QPC does not, as argued above, and further elaborated in the next section. From the perspective of the quasi-bound state scenario of Meir and collaborators, this could be phrased by saying that the conditions for the formation of a quasi-bound state cease to exist at large fields. The differences between the 0.7-anomaly and the Kondo effect are therefore evident in deviations of the QPC conductance from the Kondo predictions as  $T$  or  $B$  approaches or exceeds  $T_*$  or  $B_*$ , as already detailed in Ref. 14.

## VI. MAGNETIZATION

In the previous section we have argued that the local magnetization  $m_j$  of a KQD and QPC evolve in strikingly different ways when  $\tilde{B}$  increases far beyond  $\tilde{B}_*$  [Figures 7(e) and 7(f)]: For a KQD,  $m_j^{\text{KQD}}$  saturates in magnitude, indicating that a discrete spin is being polarized. In contrast, for a QPC,  $m_j^{\text{QPC}}$  shows no signs of saturation, indicating that a smooth redistribution of charge

and spin occurs during the polarization of the CCR. (Microscopically, this originates from differences in the  $\omega$ -dependence of the LDOS of a QD and QPC, illustrated in Fig. 3 and discussed in detail in Sec. S-4.E of Ref. 14.) To substantiate our conclusion that a QPC does not harbor a discrete, localized spin- $\frac{1}{2}$  local moment, in contrast to a KQD, we present in this section additional fRG results on the evolution, with  $\tilde{B}$  of the magnetization, conductance and charge of a KQD and QPC. For comparison, we also include fRG results for the single-impurity Anderson model (SIAM), the paradigmatic model for local moment formation in metals.<sup>38</sup> It describes a local level with energy  $\varepsilon_d = \tilde{V}_c$  and Coulomb repulsion  $U$  for double occupancy, that acquires a level width  $\Gamma$  via hybridization with a conduction band of width  $D$  (with  $D \gg U \gg \Gamma$ ).

For this purpose, we define the total charge and magnetization in the “inner” region of the CCR by

$$n_{\text{inner}} = \sum_{|j| \leq j_{\text{inner}}} n_j, \quad m_{\text{inner}} = \sum_{|j| \leq j_{\text{inner}}} m_j. \quad (11)$$

For the KQD geometry, we choose the inner region to lie

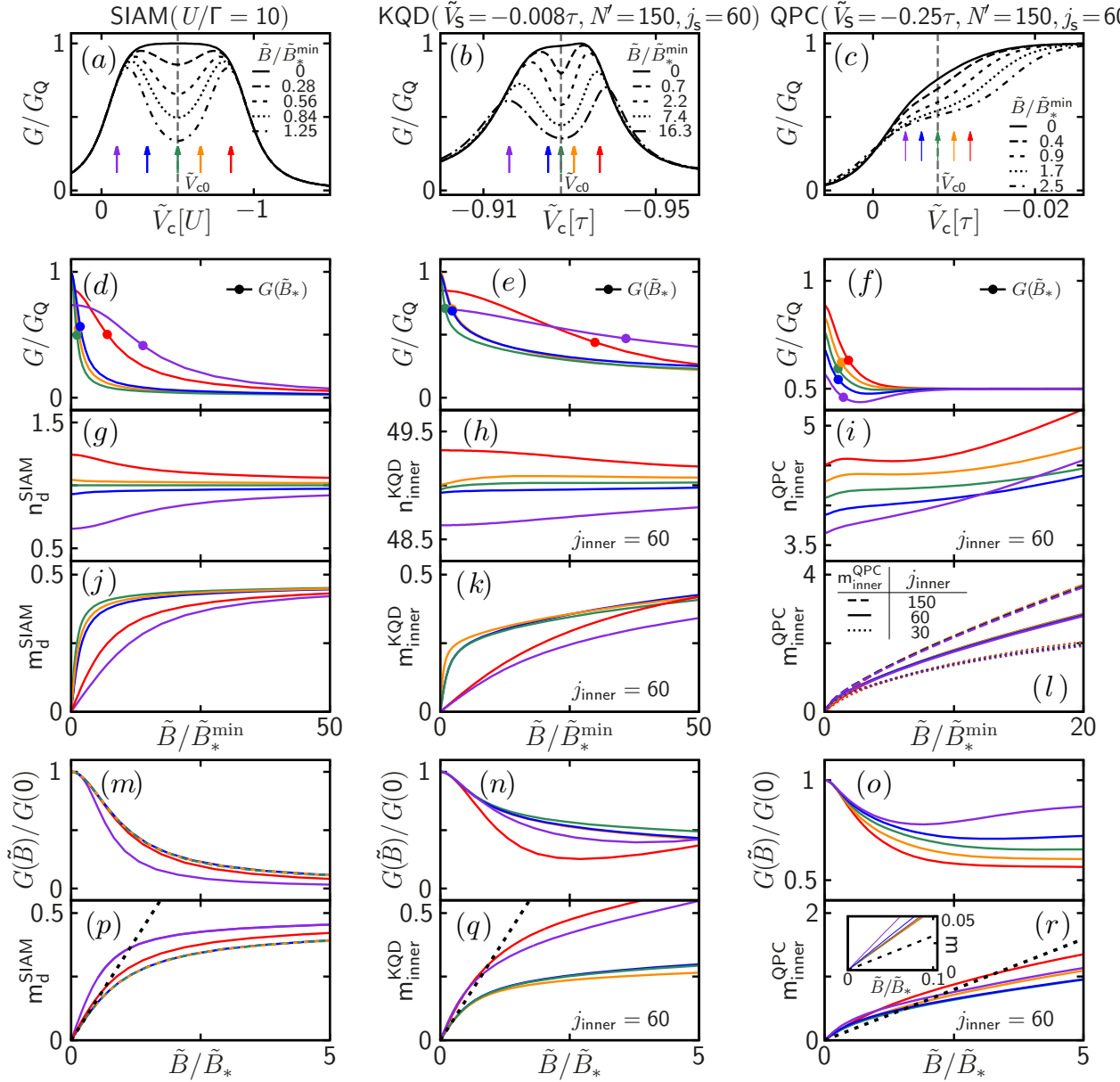


Figure 8. FRG results (with vertex flow included) for the large-field behavior of the single-impurity Anderson model (SIAM, left column), a KQD (middle column, same parameters as Fig. 6(c)), and a QPC (right column, same parameters as Fig. 6(d)). (a-c) The conductance  $G$ , plotted as function of  $\tilde{V}_c$ , for five values of magnetic field; vertical dashed lines indicate the  $\tilde{V}_c$ -value where  $\tilde{B}_*$  is minimal,  $\tilde{B}_*(\tilde{V}_{c0}) = \tilde{B}_*^{\min}$ . (d-f) The conductance, (g-i) the total charge  $n_{\text{inner}}$ , and (j-k) the total magnetization  $m_{\text{inner}}$  in the CCR's inner region, comprising sites  $|j| \leq j_{\text{inner}}$  [Eq. (11)]. These are plotted as functions of field  $\tilde{B}/\tilde{B}_*^{\min}$ , for five different values of gate voltage  $\tilde{V}_c$ , indicated by arrows of corresponding color in (a-c). (For the SIAM, the CCR consists of just a single central site, which constitutes the local d-level of that model, thus  $n_{\text{inner}}^{\text{SIAM}} = n_d^{\text{SIAM}}$  and  $m_{\text{inner}}^{\text{SIAM}} = m_d^{\text{SIAM}}$ .) (m-o) and (p-r) Same conductance and magnetization data as in (d-f) and (j-l), respectively, but plotted vs.  $\tilde{B}/\tilde{B}_*$ ; black dotted lines in (p-r) have slope  $1/\pi$ , indicating the small-field limiting behavior  $m_{\text{inner}} = \tilde{B}/(\pi\tilde{B}_*)$  expected in the Kondo limit [cf. Eq. (8)]. The inset of (r) shows a zoom of the limiting behavior for  $\tilde{B}/\tilde{B}_* \rightarrow 0$ .

between the two maxima of the KQD potential, say at  $\pm j_{\text{inner}}^{\text{KQD}}$ . The remaining CCR sites with  $j_{\text{inner}}^{\text{KQD}} < |j| \leq N'$  are excluded, since they lie outside the dot, in the CCR barrier's outer flanks. Although the contribution of each such site to the CCR's total charge or magnetization

is small, their total contribution is proportional to the length of the outer flanks, i.e. extensive, and hence should be excluded when discussing intensive dot properties. For the QPC geometry, in contrast, there is no natural separation between an inner region and the bar-

rier's outer flanks. We will show results for inner regions of three different sizes below: for fixed  $N' = 150$ , we choose  $j_{\text{inner}}^{\text{QPC}} = 150, 60$  and  $30$  (they all yield qualitatively similar results).

Fig. 8 compares the large-field behavior of the conductance, charge and magnetization of a KQD (middle column) and a QPC (right column). The left column shows corresponding quantities for the SIAM, which corresponds to a CCR with just a single site. We denote its local charge and magnetization by  $n_{\text{d}}^{\text{SIAM}}$  and  $m_{\text{d}}^{\text{SIAM}}$ , respectively.

Panels (a-c) of Fig. 8 show the conductance as function of  $\tilde{V}_c$  for SIAM, KQD and QPC, respectively, for five magnetic fields, specified in units of the  $\tilde{V}_c$ -independent reference field  $\tilde{B}_*^{\text{min}} = \min[\tilde{B}_*(\tilde{V}_c)]$  [cf. Figs. 6(c,d)]. Colored arrows indicate five fixed  $\tilde{V}_c$ -values used to calculate the corresponding curves in all other panels. These show the conductance (panels d-f), charge (panels g-i) and magnetization (panels j-l) as functions of  $\tilde{B}/\tilde{B}_*^{\text{min}}$ , as well as the scaled conductance  $G(\tilde{B})/G(0)$  (panels m-o) and magnetization (panels p-r) as functions of  $\tilde{B}/\tilde{B}_*$ . For SIAM and KQD, the blue, green and orange curves correspond to the local-moment regime [ $G/G_Q \simeq 1$  in (a,b), local charge close to 1 in (g,h)], while the red and purple curves correspond to the mixed-valence regime.

Upon comparing the three columns, we note the following salient features: (i) For all five  $\tilde{V}_c$ -values, the charges  $n_{\text{d}}^{\text{SIAM}}$ ,  $n_{\text{inner}}^{\text{KQD}}$  and  $n_{\text{inner}}^{\text{QPC}}$  all depend only weakly on  $\tilde{B}$  (g-i). In the small-field limit, the conductance and magnetization shows Fermi-liquid behavior in all cases: (ii) the conductance decreases quadratically with field (d-f), and (iii) the magnetization increases linearly with field (g-i). (iv) At intermediate fields both conductance (d-f) and magnetization (g-i) go through a crossover, during which their slopes decrease markedly in magnitude. (v) In the large-field regime beyond this crossover, the behavior of the SIAM and KQD differs strikingly from that of the QPC: SIAM and KQD exhibit behavior characteristic of a spin- $\frac{1}{2}$  local moment, whereas the QPC becomes spin-polarized with a magnetization much larger than  $\frac{1}{2}$ .

To be specific, the evidence for this interpretation of the large-field regime is as follows: (vi) For the SIAM, the plateau in  $m_{\text{d}}^{\text{SIAM}}$  saturates towards  $0.5$  (j); this saturation is the hallmark of a polarized spin- $\frac{1}{2}$  local moment. (vii) At the same time, the conductance  $G$  continues to decrease with field, albeit very slowly (d). (For the SIAM this decrease is known to be logarithmic,  $\sim 1/\ln(\tilde{B}/\tilde{B}_*)$ , but fRG is not sufficiently accurate to reproduce purely logarithmic behavior.) The KQD exhibits qualitatively similar features, though with some quantitative differences: (viii) The plateau in  $m_{\text{inner}}^{\text{KQD}}$  is fairly flat, too (k), although it does not truly saturate but instead slowly increases past  $0.5$  for sufficiently large fields. This reflects the fact that the KQD in Fig. 8 harbors not only one spin- $\frac{1}{2}$  local moment but many additional occupied levels ( $n_{\text{inner}} \simeq 50$ ); some of these begin to contribute to

the magnetization when  $\tilde{B}$  becomes a sufficiently large fraction of the dot level spacing. (ix) The KQD conductance continues to decrease with field (e), but less slowly so than for the SIAM (d), due to contributions from the additional levels.

The above large-field features of the SIAM and a KQD stand in stark contrast to those of a QPC: (x) its magnetization continues to increase with field without any saturation (l) [the slope depends on the width of the inner region: the larger  $j_{\text{inner}}$ , the larger the slope]; and (xi) the conductance fully saturates at  $G = 0.5G_Q$  (f), corresponding to a spin-split conductance plateau. The absence of any saturation in the magnetization reflects the fact that the QPC barrier lacks the isolated ‘‘inner region’’ of a KQD. Instead, the CCR barrier is made up entirely of outer flanks, along which electrons of both spin species can freely move. As the magnetic field is increased, the magnetization of the QPC is thus free to increase without any intrinsic limit (in contrast to the case of a KQD). The spin-split conductance plateau sets in once the LDOS at the chemical potential is fully spin-polarized.

These differences between SIAM and KQD on the one hand and QPC on the other of course imply different behaviors when the conductance and magnetization are plotted versus  $\tilde{B}/\tilde{B}_*$ : (xii) For the local-moment curves (blue, green, orange) of the SIAM, the scaled conductance  $G(\tilde{B})/G(0)$  (m) and the magnetization (p) both collapse onto a single scaling curve when plotted versus  $\tilde{B}/\tilde{B}_*$ . (xiii) The same is true approximately for the KQD's conductance (n) and magnetization (q), though the collapse is not as perfect. Thus, for the SIAM and KQD, the  $\tilde{V}_c$ -dependent scale  $\tilde{B}_*$  governs both the small- and large-field behavior of the magnetization and conductance. (xiv) This is not the case for the QPC, whose conductance (o) and magnetization (r) do *not* show a collapse onto a single curve when plotted versus  $\tilde{B}/\tilde{B}_*$ . (xv) Instead, the large-field behavior of the magnetization is governed by a  $\tilde{V}_c$ -independent scale: when the  $m_{\text{inner}}^{\text{QPC}}$ -curves are plotted vs.  $\tilde{B}/\tilde{B}_*^{\text{min}}$ , they all overlap (l), except in the limit  $\tilde{B} \ll \tilde{B}_*^{\text{min}}$  [not resolved in (l)]. Also, (xvi) the field scale at which the conductance saturates at  $G = 0.5G_Q$  does not depend on  $\tilde{B}_*$  at all, but instead grows linearly with decreasing  $\tilde{V}_c$  (f).

To summarize: when the SIAM and the KQD are tuned into their local moment regime, their conductance and magnetization exhibit the expected crossover, governed only by a single energy scale  $\tilde{B}_*(\tilde{V}_c)$ , between a Fermi-liquid and a local-moment fixed point that is characteristic of the Kondo effect, (xii,xiii). The QPC conductance and magnetization, however, do not, (xiv-xvi). This is an example, therefore, where the analogy between Kondo effect and 0.7-anomaly breaks down – at large fields, they are distinct physical effects.

The lack of local-moment behavior for the QPC magnetization at large fields is not surprising, given the open nature of the QPC geometry. Nevertheless – and this is

surprising and remarkable – (xvii) the small-field limit ( $\tilde{B} \ll \tilde{B}_*$ ) of the magnetization is governed by  $\tilde{B}_*$  not only for the SIAM and KQD in the local moment regime, but also for the QPC when  $\tilde{V}_c < \tilde{V}_{c0}$ : For all these, the *linear* response of the magnetization to field is proportional to  $1/\tilde{B}_*$ , meaning that curves of  $m_{\text{inner}}$  vs.  $\tilde{B}/\tilde{B}_*$  for different  $\tilde{V}_c$ -values all have the same slope as  $\tilde{B}/\tilde{B}_* \rightarrow 0$ . [This is illustrated by the blue, green, orange lines in panels (p) and (q), which all have slope  $1/\pi$  (dashed black line), in accord with Eq. (8); and by the green, orange and red curves in the inset of panel (r), which have mutually similar slopes, though these do not equal  $1/\pi$  (dashed black line).] The fact that the small-field limit of the QPC magnetization is governed by  $\tilde{B}_*$ , (xvii) has far-reaching consequences, in that it underlies the low-energy Fermi-liquid behavior of the QPC conductance mentioned in Sec. IV C above.

We end this subsection with a parenthetic remark: As an alternative to Eq. (11), outer flank contributions to the magnetization can also be eliminated by considering

$$m_{\text{exc}}(\tilde{V}_c) = \sum_{j \in \text{CCR}} m_j(\tilde{V}_c) - \sum_{j \in \text{CCR}} m_j(\tilde{V}_c^{\text{ref}}), \quad (12)$$

the excess magnetization of the CCR at central gate voltage  $\tilde{V}_c$  relative to its magnetization at a suitably chosen reference voltage  $\tilde{V}_c^{\text{ref}}$  [chosen to define an even QD (EQD) in an Coulomb blockade value adjacent to the odd KQD, or an open QPC, as discussed in conjunction with Eq. (9)]. Indeed, for small fields ( $\tilde{B}/\tilde{B}_* \ll 1$ ) one finds  $m_{\text{exc}}(\tilde{B}) \simeq m_{\text{inner}}(\tilde{B})$  when choosing  $j_{\text{inner}} = j_s$ , and the excess susceptibility defined in Eq. (9) corresponds to  $\chi_{\text{exc}} = (\partial m_{\text{exc}}/\partial \tilde{B})_{\tilde{B}=0}$ . However, for the large-field regime of interest in the present subsection, the subtraction scheme of Eq. (12) is not convenient, because at sufficiently large fields the second term becomes comparable in size to the first, causing  $m_{\text{exc}}$  to decrease.

## VII. SUMMARY AND OUTLOOK

In Ref. 14, we have argued that the .7KS, i.e. the observed similarities in the low-energy behavior of the conductance for 0.7-anomaly and the Kondo effect, originate from geometry-induced, interaction-enhanced local spin fluctuations, that are present both in a QPC and a KQD. The goal of the present work has been to offer additional evidence for this conclusion, by studying the geometric crossover between a QD and a QPC, both experimentally and theoretically, focusing on the magnetic field dependence at low temperatures. Our experimental and numerical results were found to be in good qualitative agreement. This shows that the 1D-model with short-range interactions introduced here, together with the fRG approach used to treat interactions, succeeds in capturing the essential physics of the Kondo effect, the 0.7-anomaly and the geometric crossover between them.

Our initial motivation for studying the geometric crossover was the expectation that this would allow us to observe an adiabatic transition from Kondo correlations present in a KQD to the correlations present in a QPC showing the 0.7-anomaly. Indeed, this idea turned out to be fruitful: our fRG results show that an anomalously strong negative magnetoconductance, one of the key features of the .7KS, always goes hand in hand with strongly enhanced local spin fluctuations.

The spatial structure of the local spin fluctuations is inherited from that of the non-interacting local density of states at the chemical potential, and enhanced by interactions in Stoner-type fashion. Roughly speaking, local spin fluctuations are strong in those regions of space where the electrons near the chemical potential are “slow”. For a parabolic QPC, slow electrons are found in the CCR when the barrier top is just below the chemical potential, whereas for a KQD the odd electron is slow simply because it is really trapped inside the dot. The difference between these two situations does not matter much for low energies ( $\ll |\tilde{B}_*|$ ), thus both show behavior characteristic of a Nozières-Fermi liquid with local interactions. (These local interactions are the reason why the .7KS also comprises similar temperature and source-drain voltage dependences for a KQD and a QPC, see Ref. 14 for a more detailed discussion of this point.) The difference does matter, though, for high energies, where we find no indications that a parabolic QPC harbors a localized state, and where indeed no .7KS is observed.

One of the lessons learnt from Figs. 7(i-l) is that the presence or absence of the two crucial properties discussed above, namely a strong negative magnetoconductance and strong local spin fluctuations, depends very much on the trajectory followed in the  $(\tilde{V}_c, \tilde{V}_s)$  plane during the QD-QPC crossover. For example, for the trajectory studied in Fig. 7(k), *both* these features disappear in the intermediate regime between the KQD and the QPC, because there the barrier top is so far below the chemical potential that the system is essentially an open channel, with  $g \simeq 1$ .

It is, of course, possible to also implement QD-QPC crossover trajectories during which the barrier top always remains close to the chemical potential. Suppose that such a trajectory includes a wide, flat barrier top, such as that shown in Fig. 3(b). When this barrier top is just below the chemical potential, the electron density will be low throughout the wide barrier region, implying that interaction effects will become very strong there. This regime is conducive to the formation of a Wigner crystal, so that the conductance can be expected to show behavior different from that of a “standard” 0.7-anomaly. Indeed two recent experimental papers have studied this regime<sup>32,33</sup> and reported interesting differences from standard 0.7-phenomenology (such as a zero-bias peak that splits into two or even three subpeaks as the barrier width is varied).

In our own detailed studies of QPCs, both in Ref. 14 and here, we have so far purposefully chosen to avoid the



regime of wide, flat barrier tops. Instead, we have focussed on parabolic barrier tops and demonstrated that these were sufficient to explain numerous features of the standard 0.7-anomaly. Nevertheless, it would be very interesting to systematically study the crossover from parabolic to wide, flat barrier tops. The latter lead to Fabry-Perot resonances even in the absence of interactions (as argued in Sec. III C), and the way in which Fabry-Perot structures in the density of states are modified or enhanced by interactions has not been explored systematically yet.

In the limit of a very wide and flat barrier, the CCR would represent a long 1D wire of low density, behaving as a spin-incoherent Luttinger liquid<sup>39</sup>. Since interaction effects become ever more important as the density decreases, fRG will at some point become unsuitable for a flat barrier top when either its width is made sufficiently wide or its top approaches the chemical potential sufficiently closely from below. However, more powerful numerical methods, such as the density matrix renormalization group, could be used to study such situations.

### ACKNOWLEDGEMENTS

We thank B. Altshuler, P. Brouwer, R. Egger, J. Folk, L. Glazman, V. Golovach, A. Högele, Y. Imry, M. Kiselev, D. Logan, D. Loss, C. Marcus, Y. Meir, M. Pustilnik, A. Rosch, H. Sellier, K. Schönhammer, B. Spivak and A. Yacoby for stimulating discussions, and in particular S. Andergassen, C. Honerkamp, S. Jakobs, C. Karrasch, V. Meden, M. Pletyukhov and H. Schoeller for fRG-related help and advice. We also thank Christoph Hohmann for producing Figs. 1(b),(c). We acknowledge support from the DFG via SFB-631, SFB-TR12, De730/3-2, De730/4-1, De730/4-2, De730/4-3, HO 4687/1-3, LU819/4-1, and the Cluster of Excellence *Nanosystems Initiative Munich*, and the National Science Foundation under Grant No. NSF PHY05-51164. S.L. acknowledges support via a Heisenberg fellowship of the DFG.

### Appendix A: Evolution of $g(\tilde{V}_c, \tilde{V}_s)$ with $\tilde{B}$ (movie)

In Sec. IV A, we showed fRG results (without vertex flow) for the QD-to-QPC crossover of the conductance  $g(\tilde{V}_c, \tilde{V}_s)$  as function of central and side gate voltage, for three values of magnetic field [Figs. 5(a-c)]. Its continuous evolution with  $\tilde{B}$ , again calculated by fRG without vertex flow, can be viewed as a QuickTimas a separate figure as a separate figure Movie, see the file “fRG.mov” in the Supplementary Material. The movie shows simultaneously the evolution with  $\tilde{B}$  of three data sets: The central panel gives the conductance  $g(\tilde{V}_c, \tilde{V}_s)$  in a three-dimensional plot formatted in the same way as Figs. 5(a-c). The top left panel gives the frontmost curve of the central panel,  $g(\tilde{V}_c, \tilde{V}_s = 0.018\tau)$ , representing the

pure QD regime; and the top right panel gives its backmost curve  $g(\tilde{V}_c, \tilde{V}_s = 1.9\tau)$ , representing the pure QPC regime. A moving horizontal line in the scale bar on the right hand side indicates the evolution of  $\tilde{B}$ , and whenever it passes one of a selected set of  $\tilde{B}$  values, that value is indicated by a frozen horizontal line, while two curves of matching color freeze in the top left and top right panels.

The initial evolution for small fields ( $\tilde{B} \lesssim 2 \times 10^{-4}\tau$ ) shows how the Kondo plateaus of the first few Kondo valleys, whose typical Kondo temperatures increase with dot occupancy  $n$ , successively get suppressed as  $\tilde{B}$  increases [see top left panel]. For larger fields ( $\tilde{B} \gtrsim 2 \times 10^{-4}$ ), the conductance in the QPC regime also begins to develop a shoulder [see top right panel], which evolves (beyond  $\tilde{B} \gtrsim 3 \times 10^{-3}$ ) into an ever more pronounced double step. Note that the scale bar changes from logarithmic to linear at  $\tilde{B} \simeq \times 10^{-4}$ , since the  $\tilde{B}$ -dependence of the conductance at large fields is logarithmic for the Kondo effect, but linear for the 0.7-anomaly. (This is another indication that the latter does not involve local-moment physics at large fields.)

For large magnetic fields (beyond about  $\tilde{B} \gtrsim 10^{-4}$ ) the movie shows several sharp conductance resonances or peaks of height  $g \simeq 1$ , which move in the direction of decreasing  $\tilde{V}_c$  (toward the right) with increasing magnetic field. An example of such a resonance, occurring for  $\tilde{B} = 1.4 \cdot 10^{-3}\tau$  and  $\tilde{V}_s = 0.018\tau$  at  $\tilde{V}_c = 0.01303\tau$ , is shown in Fig. 9. We will call these “spin-flip resonances”, since their origin lies in spin-flip transitions on the QD; in fact, they can be viewed as generalized versions of the singlet-triplet Kondo effect discussed in the literature (see Ref. 40, and references therein). Although the spin-flip resonances have no relevance for the 0.7-anomaly, they are interesting in their own right, hence we now explain their origin in some more detail.

With increasing magnetic field, the total spin of a Coulomb-blockaded QD will increase in discrete steps. This has been discussed in the past in terms of the Fock-Darwin spectrum of a QD, see e.g. Fig. 5 in Ref. 41. Such a step involves adding a spin-up electron to the lowest-lying empty dot level while removing a spin-down electron from the highest-lying doubly-occupied one, which occurs whenever the gain in Zeeman energy outweighs the cost in kinetic energy. The latter depends on the QD’s level spacing, and hence on  $\tilde{V}_c$  and  $\tilde{V}_s$ . For given  $\tilde{B}$  and  $\tilde{V}_s$ , such a transition can thus also be induced changing  $\tilde{V}_c$ . To be specific, decreasing  $\tilde{V}_c$  (as in Fig. 9) increases the level spacing and causes a spin-decreasing spin-flip transition, say from the dot configuration  $(n_{\uparrow}^{\text{QD}}, n_{\downarrow}^{\text{QD}})$  to  $(n_{\uparrow}^{\text{QD}} - 1, n_{\downarrow}^{\text{QD}} + 1)$ . Precisely at the spin-flip transition, say for  $\tilde{V}_c = \tilde{V}_c^{\text{flip}}$ , these two configurations are energetically degenerate, so that Kondo-like correlations between the QD and the leads can develop, which cause the conductance  $g$  to reach its maximum possible value, namely 1.

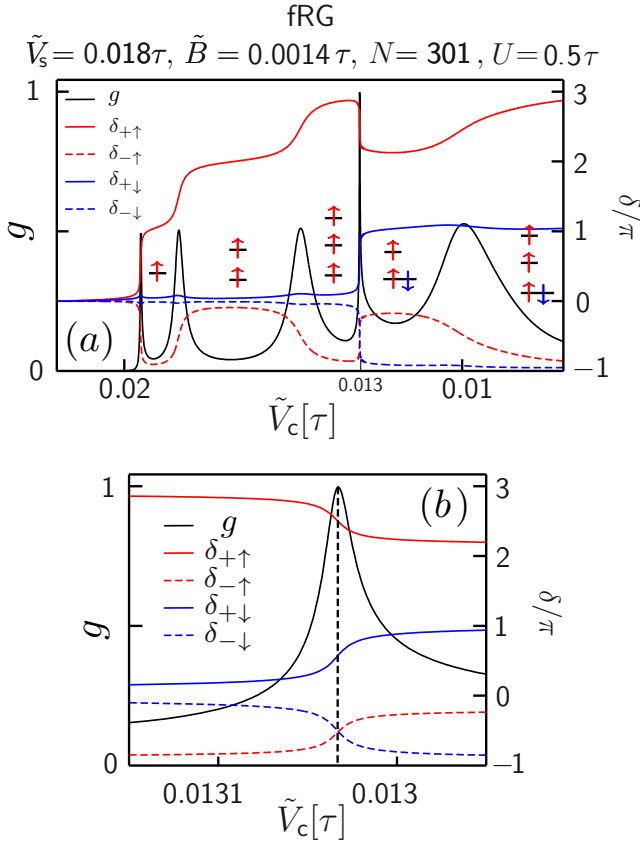


Figure 9. Example of a spin-flip resonance in the conductance of a QD. (a) Conductance (solid black line) and phases  $\delta_{\sigma,+}/\pi = n_{\sigma}^{\text{QD}}$  (solid lines) and  $\delta_{\sigma,-}/\pi$  (dashed lines), for  $\sigma = \uparrow$  (red lines) and  $\sigma = \downarrow$  (blue lines), all calculated using fRG. The phases are all set to 0 at a reference voltage  $\tilde{V}_c^r = 0.022$  so large that the CCR no longer represents a QD, but a pinched-off QPC, with  $g = 0$  and  $n_{\sigma}^{\text{QD}} = 0$ . As  $\tilde{V}_c$  decreases below  $0.02\tau$  where the dot is still empty,  $n_{\uparrow}^{\text{QD}}$  (red solid line) initially increases in roughly integer steps as the dot is being charged, while  $n_{\downarrow}^{\text{QD}}$  (blue solid line) stays essentially zero, because the fixed field  $\tilde{B}$  is large. However at  $\tilde{V}_c^{\text{flip}} = 0.01303\tau$  (vertical dashed line) a spin-flip transition occurs, where  $(n_{\uparrow}^{\text{QD}}, n_{\downarrow}^{\text{QD}})$  changes from  $\simeq (3, 0)$  to  $\simeq (2, 1)$ , and the conductance shows a spin-flip resonance of height 1. (b) Zoom-in of the same data to the vicinity of the spin-flip transition at  $\tilde{V}_c^{\text{flip}}$ .

In the movie the heights of these spin-flip resonances typically do not reach unity, but rather fluctuate as a function of magnetic field. This is a numerical artefact caused by the insufficient resolution of  $\tilde{V}_c$  used when making the movie. The numerical effort that would have been needed to resolve these type of resonances in the movie would have been very high, since they are typically very narrow. (We note also that at finite temperature, the minimum width of these resonances would be set by temperature.)

The fact that  $g = 1$  at a spin-flip resonance can be understood, following Ref. 40, using elementary concepts from the Fermi-liquid description of zero-temperature transport through a multi-level quantum dot. (For present purposes, we call the entire CCR a ‘‘QD’’). Such a description is formulated in terms of the eigenphases, say  $\delta_{\sigma,1}$  and  $\delta_{\sigma,2}$ , of the scattering matrix of the QD. (A detailed discussion of how these eigenphases can be calculated using fRG is given in our follow-up paper<sup>42</sup>.) These eigenphases are defined w.r.t. a reference gate voltage  $\tilde{V}_c^r$ , at which we set  $\delta_{\sigma,1} = \delta_{\sigma,2} = 0$ . The even and odd linear combinations of these eigenphases,

$$\delta_{\sigma,\pm} = \delta_{\sigma,1} \pm \delta_{\sigma,2}, \quad (\text{A1})$$

determine, respectively, the quantum dot’s charge  $n^{\text{QD}}$  and conductance  $g$ . The charge  $n^{\text{QD}}$ , measured w.r.t. the reference point, is given by Friedel’s sum rule:

$$n^{\text{QD}} = n_{\uparrow}^{\text{QD}} + n_{\downarrow}^{\text{QD}} = \frac{1}{\pi} (\delta_{\uparrow,+} + \delta_{\downarrow,+}). \quad (\text{A2})$$

The conductance is given by the relation

$$g = \frac{1}{2} \sum_{\sigma} \sin^2 \delta_{\sigma,-}, \quad (\text{A3})$$

valid for left-right symmetric couplings between QD and leads, as in our model. We choose  $\tilde{V}_c^r$  to lie near the spin-flip transition, but sufficiently different from  $\tilde{V}_c^{\text{flip}}$  that the conductance and the phases determining it are small at  $\tilde{V}_c^r$ , i.e.  $g \ll 1$  and  $|\delta_{\sigma,-}| \ll \pi/2$ .

Now, when  $\tilde{V}_c$  is tuned through the spin-flip transition, the  $\tilde{V}_c$ -induced changes in  $\delta_{\sigma,-}$  and  $n_{\sigma}^{\text{QD}}$  (w.r.t. to their values, namely 0, at the reference voltage  $\tilde{V}_c^r$ ) are related by

$$\Delta \delta_{\sigma,-} \simeq \pi \Delta n_{\sigma}^{\text{QD}}. \quad (\text{A4})$$

This equation follows from two facts: first, one of the spin-dependent eigenphases of the scattering matrix, either  $\delta_{\sigma,1}$  or  $\delta_{\sigma,2}$ , turns out to be essentially independent of  $\tilde{V}_c$  throughout a Coulomb-blockade valley, so that  $|\Delta \delta_{\sigma,-}| = |\Delta \delta_{\sigma,+}|$  [by Eq. (A1)]; second, the Friedel sum rule implies that  $\Delta \delta_{\sigma,+} = \pi \Delta n_{\sigma}^{\text{QD}}$ . Now, since the total dot charge  $n^{\text{QD}} = n_{\uparrow}^{\text{QD}} + n_{\downarrow}^{\text{QD}}$  is fixed within the Coulomb blockade valley, the spin-dependent dot occupancies change in equal but opposite manner as  $\tilde{V}_c$  is tuned through the spin-flip transition:  $\Delta n_{\uparrow}^{\text{QD}} \simeq -\Delta n_{\downarrow}^{\text{QD}}$ . By Eq. (A4), this implies that both  $|\Delta \delta_{\uparrow,-}|$  and  $|\Delta \delta_{\downarrow,-}|$  will pass through  $\pi/2$  at essentially the same value of  $\tilde{V}_c$ , causing the conductance  $g$  [Eq. (A3)] to show a resonance of height  $\simeq 1$  there. The case shown Fig. 9 is an example of a so-called ‘‘triplet-singlet’’ transition<sup>40</sup>, where the spin of the QD changes from  $3/2$  to  $1/2$  as  $\tilde{V}_c$  decreases past  $\tilde{V}_c^r$ .

- <sup>1</sup> B. J. van Wees, H. van Houten, C. W. J. Beenakker, J. G. Williamson, L. P. Kouwenhoven, D. van der Marel, and C. T. Foxon, *Phys. Rev. Lett.* **60**, 848 (1988).
- <sup>2</sup> D. A. Wharam, T. J. Thornton, R. Newbury, M. Pepper, H. Ahmed, J. E. F. Frost, D. G. Hasko, D. C. Peacock, D. A. Ritchie, and G. A. C. Jones, *Journal of Physics C: Solid State Physics* **21**, L209 (1988).
- <sup>3</sup> M. Büttiker, *Phys. Rev. B* **41**, 7906 (1990).
- <sup>4</sup> K. J. Thomas, J. T. Nicholls, M. Y. Simmons, M. Pepper, D. R. Mace, and D. A. Ritchie, *Phys. Rev. Lett.* **77**, 135 (1996).
- <sup>5</sup> K. J. Thomas, J. T. Nicholls, N. J. Appleyard, M. Y. Simmons, M. Pepper, D. R. Mace, W. R. Tribe, and D. A. Ritchie, *Phys. Rev. B* **58**, 4846 (1998).
- <sup>6</sup> D. J. Reilly, G. R. Facer, A. S. Dzurak, B. E. Kane, R. G. Clark, P. J. Stiles, R. G. Clark, A. R. Hamilton, J. L. O'Brien, N. E. Lumpkin, L. N. Pfeiffer, and K. W. West, *Phys. Rev. B* **63**, 121311(R) (2001).
- <sup>7</sup> S. M. Cronenwett, H. J. Lynch, D. Goldhaber-Gordon, L. P. Kouwenhoven, C. M. Marcus, K. Hirose, N. S. Wingreen, and V. Umansky, *Phys. Rev. Lett.* **88**, 226805 (2002).
- <sup>8</sup> Y. Chung, S. Jo, D.-I. Chang, H.-J. Lee, M. Zaffalon, V. Umansky, and M. Heiblum, *Phys. Rev. B* **76**, 035316 (2007).
- <sup>9</sup> E. Koop, A. Lerescu, J. Liu, B. van Wees, D. Reuter, A. D. Wieck, and C. van der Wal, *J. Supercond. Nov. Magn.* **20**, 433 (2007).
- <sup>10</sup> M. Pepper and J. Bird, *J. Phys. Cond. Mat.* **20**, 160301 (2008).
- <sup>11</sup> S. Nakamura, M. Hashisaka, Y. Yamauchi, S. Kasai, T. Ono, and K. Kobayashi, *Phys. Rev. B* **79**, 201308 (2009).
- <sup>12</sup> Y. Komijani, M. Csontos, I. Shorubalko, T. Ihn, K. Ensslin, Y. Meir, D. Reuter, and A. D. Wieck, *Eur. Phys. Lett.* **91**, 67010 (2010).
- <sup>13</sup> L. W. Smith, A. R. Hamilton, K. J. Thomas, M. Pepper, I. Farrer, J. P. Griffiths, G. A. C. Jones, and D. A. Ritchie, *Phys. Rev. Lett.* **107**, 126801 (2011).
- <sup>14</sup> F. Bauer, J. Heyder, E. Schubert, D. Borowsky, D. Taubert, B. Bruognolo, D. Schuh, W. Wegscheider, J. von Delft, and S. Ludwig, *Nature* **501**, 73 (2013).
- <sup>15</sup> L. Glazman and M. Raikh, *JETP Lett.* **47**, 452 (1988).
- <sup>16</sup> T. K. Ng and P. A. Lee, *Phys. Rev. Lett.* **61**, 1768 (1988).
- <sup>17</sup> D. Goldhaber-Gordon, H. Shtrikman, D. Mahalu, D. Abusch-Magder, U. Meirav, and M. A. Kastner, *Nature* **391**, 156 (1998).
- <sup>18</sup> S. M. Cronenwett, T. H. Oosterkamp, and L. P. Kouwenhoven, *Science* **281**, 540 (1998), <http://www.sciencemag.org/cgi/reprint/281/5376/540.pdf>.
- <sup>19</sup> W. G. van der Wiel, S. D. Franceschi, T. Fujisawa, J. M. Elzerman, S. Tarucha, and L. P. Kouwenhoven, *Science* **289**, 2105 (2000), <http://www.sciencemag.org/cgi/reprint/289/5487/2105.pdf>.
- <sup>20</sup> J. Nygard, D. H. Cobden, and P. E. Lindelof, *Nature* **408**, 342 (2000).
- <sup>21</sup> P. Jarillo-Herrero, J. Kong, H. S. van der Zant, C. Dekker, L. P. Kouwenhoven, and S. De Franceschi, *Nature* **434**, 484 (2005).
- <sup>22</sup> A. V. Kretinin, H. Shtrikman, D. Goldhaber-Gordon, M. Hanl, A. Weichselbaum, J. von Delft, T. A. Costi, and D. Mahalu, *Phys. Rev. B* **84**, 245316 (2011).
- <sup>23</sup> Y. Meir, K. Hirose, and N. S. Wingreen, *Phys. Rev. Lett.* **89**, 196802 (2002).
- <sup>24</sup> A. Golub, T. Aono, and Y. Meir, *Phys. Rev. Lett.* **97**, 186801 (2006).
- <sup>25</sup> T. Rejec and Y. Meir, *Nature* **442**, 900 (2006).
- <sup>26</sup> P. Nozières, *J. Low Temp. Phys.* **17**, 31 (1974).
- <sup>27</sup> F. D. M. Haldane, *Phys. Rev. Lett.* **40**, 416 (1978).
- <sup>28</sup> S. Andergassen, T. Enss, V. Meden, W. Metzner, U. Schollwöck, and K. Schönhammer, *Phys. Rev. B* **73**, 045125 (2006).
- <sup>29</sup> C. Karrasch, T. Enss, and V. Meden, *Phys. Rev. B* **73**, 235337 (2006).
- <sup>30</sup> W. Metzner, M. Salmhofer, C. Honerkamp, V. Meden, and K. Schönhammer, *Rev. Mod. Phys.* **84**, 299 (2012).
- <sup>31</sup> F. Bauer, J. Heyder, and J. von Delft, *Phys. Rev. B* **89**, 045128 (2014).
- <sup>32</sup> M. J. Iqbal, R. Levy, E. J. Koop, J. B. Dekker, J. P. de Jong, J. H. M. van der Velde, D. Reuter, A. D. Wieck, R. Aguado, Y. Meir, and C. H. van der Wal, *Nature* **501**, 79 (2013).
- <sup>33</sup> B. Brun, F. Martins, S. Faniel, B. Hackens, G. Bachelier, A. Cavanna, C. Ulysse, A. Ouerghi, U. Gennser, D. Mailly, S. Huant, V. Bayot, M. Sanquer, and H. Sellier, *Nature Comm.* **5**, 4290 (2014).
- <sup>34</sup> T. A. Costi, *Phys. Rev. B* **64**, 241310 (2001).
- <sup>35</sup> L. Glazman and M. Pustilnik, in *Nanophysics: Coherence and Transport*, edited by H. Bouchiat and *et al.* (Elsevier, Amsterdam, 2005) pp. 427–478, cond-mat/0501007.
- <sup>36</sup> D. M. Schröer, A. K. Hüttel, K. Eberl, S. Ludwig, M. N. Kiselev, and B. L. Altshuler, *Phys. Rev. B* **74**, 233301 (2006).
- <sup>37</sup> S. Ihnatsenka and I. V. Zozoulenko, *Phys. Rev. B* **76**, 045338 (2007).
- <sup>38</sup> P. W. Anderson, *Phys. Rev.* **124**, 41 (1961).
- <sup>39</sup> K. A. Matveev, *Phys. Rev. B* **70**, 245319 (2004).
- <sup>40</sup> M. Pustilnik, L. I. Glazman, and W. Hofstetter, *Phys. Rev. B* **68**, 161303 (2003).
- <sup>41</sup> L. P. Kouwenhoven, D. G. Austing, and S. Tarucha, *Reports on Progress in Physics* **64**, 701 (2001).
- <sup>42</sup> J. von Delft, F. Bauer, and J. Heyder, to be published (2014).